J Eng Math (2007) 62:103–131
DOI 10.1007/s10665-007-9178-y

Kinematic instabilities in two-layer eccentric annular flows, part 1: Newtonian fluids

Miguel A. Moyers-Gonzalez · Ian A. Frigaard

Received: 27 October 2006 / Accepted: 4 May 2007 / Published online: 17 August 2007

Abstract Primary-cementing displacement flows occur in long narrow eccentric annuli during the construction of oil and gas wells. A common problem is that the displacing fluid fingers up the upper wide side of the annulus, leaving behind a "mud channel" of displaced fluid on the lower narrow side of the annulus. Tehrani et al. report that the interface between displacing fluid and mud channel can in certain circumstances become unstable, and a similar phenomenon has been observed in our ongoing experiments. Here an explanation for these instabilities is provided via analysis of the stability of two-layer eccentric annular Hele-Shaw flows, using a transient version of the usual Hele-Shaw approach, in which fluid acceleration terms are retained. Two Newtonian fluids are considered, as a simplification of the general case in which the fluids are shear-thinning yield-stress fluids. It is shown that negative azimuthal buoyancy gradients are in general stabilizing in inclined wells, but that buoyancy may also have a destabilizing effect via axial buoyancy forces that influence the base-flow interfacial velocity. In a variety of special cases where buoyancy is not dominant, it is found that instability is suppressed by a positive product of interfacial velocity difference and reduced Reynolds-number difference between fluids. Even a small positive azimuthal buoyancy gradient, (heavy fluid over light fluid), can be stabilized in this way. Eccentricity of the annulus seems to amplify the effect of buoyancy on stability or instability, e.g. stably stratified fluid layers become more stable as the eccentricity is increased.

Keywords Hele-Shaw flow · Interfacial instability · Kinematic instability · Multi-layer flow stability · Primary cementing

1 Introduction

Primary cementing is a critically important operation in the construction of any oil or gas well, [1,2]. In this process, a steel casing is cemented into the borehole by pumping a sequence of fluids, (e.g. wash, spacer, cement slurry),

M. A. Moyers-Gonzalez
Département de mathématiques et de statistique, Université de Montréal, CP 6128 succ, Centre-Ville Montréal, QC, Canada H3C 3J7
e-mail: moyers@dms.umontreal.ca

I. A. Frigaard (✉)
Department of Mathematics and Mechanical Engineering, University of British Columbia, 2054-6250 Applied Science Lane, Vancouver, BC, Canada V6T 1Z4
e-mail: frigaard@mech.ubc.ca

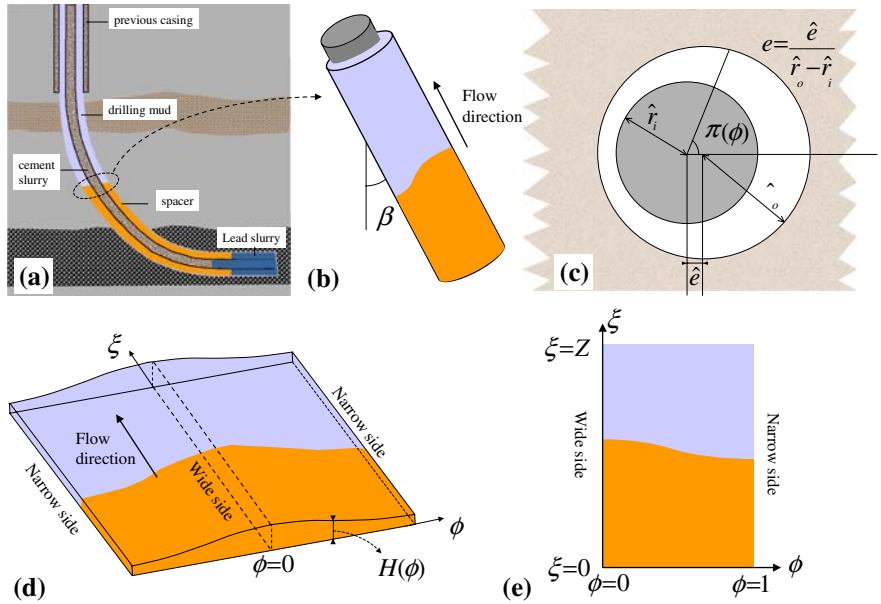

Fig. 1 Cementing geometries: (**a**) schematic of fluid stages pumped during a primary-cementing operation; (**b**) uniform section of eccentric annulus; (**c**) eccentric annular cross-section; (**d**) periodic eccentric annular Hele-Shaw cell; (**e**) final computational domain, assuming symmetry at wide and narrow sides of the annulus

down the inside of the casing, returning upwards in the annulus; see Fig. 1. The purpose of this operation is to provide a continuous impermeable hydraulic seal in the annulus, preventing any uncontrolled flow of reservoir fluids behind the casing. Many serious problems can arise from uncontrolled flows and these are discussed in [3, Chapter 5], as well as more widely in the technical literature and in our previous work [4–7].

One common cause of incomplete zonal isolation is that the cement, which is placed in the annulus between the outside of the casing and the inside of the hole, fails to fully displace the drilling mud that initially occupies this space. Most commonly, a channel of mud can be left behind on the narrow (lower) side of the annulus [8–10]. As the cement sets, the mud channel becomes dehydrated and porous, allowing reservoir fluids to flow behind the casing along the annulus.

In order to study such flows and related process problems, we have developed a Hele-Shaw modelling approach in [4–7,11,12]. In this approach the narrow annulus is unwrapped into an eccentric annular Hele-Shaw cell, see Fig. 1, resulting in a two-dimensional (2D) description of the displacement. This results in considerable simplification for both analysis and computation over, say, a 3D Navier–Stokes model, and we have been able to derive a number of useful practical results.

In the simplest model the classical Hele-Shaw approach is adopted and all inertial effects are neglected, see [4–7]. This gives a model that is useful for simulation of laminar cementing displacements, as has been shown in [4,6], and engineering software based on this type of model is currently used in the field for primary cementing design.[1] For these models we can identify parameter ranges for which there is a steady displacement front that advances as a travelling wave along the well. For some restricted parameter ranges we are even able to provide an analytical description of the steady-state shape, (concentric and mildly eccentric annuli); see [5].

If there is no steadily advancing front we can identify two possibilities: (i) that an unsteady displacement front advances along the wide side of the annulus, and (ii) that the displaced fluid becomes stuck on the narrow side of the annulus. Thus, assuming that no local interfacial instabilities occur, we may qualitatively divide the parameter space of a simple eccentric annular displacement into the three characteristic observed behaviours: steady travelling

[1] For example, see the Wellclean II simulator developed at Schlumberger: www.slb.com.

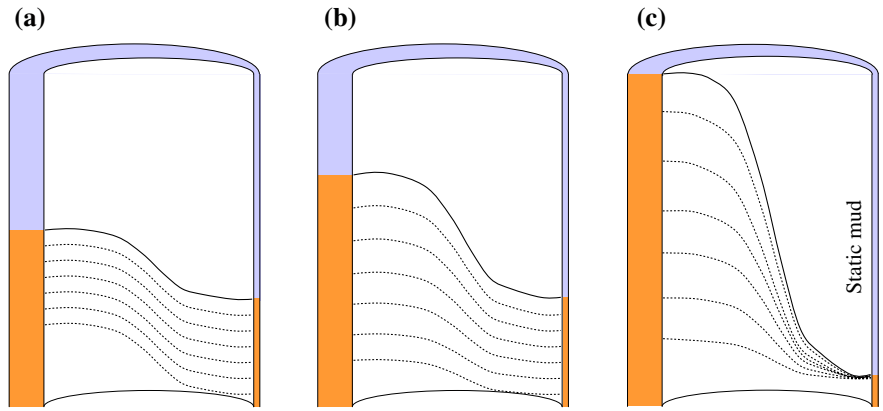

Fig. 2 Characteristic displacement behaviours: (**a**) steady travelling wave; (**b**) unsteady fingering; (**c**) static narrow side channel

Fig. 3 Illustration of a typical unsteady fingering displacement carried out in the 6 m flow loop at UBC, using two Carbopol solutions of different concentrations

wave, unsteady, static narrow side channel; see Fig. 2. These characteristic interfacial behaviours are also observable experimentally, as illustrated in Fig. 3. Predicting which occurs can be done either via simulation, as in [4,6], or by using a semi-analytic lubrication-modelling approach, as in [7]. Experimental validation of these models is underway.

From an idealistic point of view, only the steady travelling-wave solutions represent "good" displacements from the industrial perspective. Whilst a stationary channel of drilling mud on the narrow side of the annulus is certainly a serious problem, the intermediate stage of an unsteady but mobile displacement is less easy to interpret. An unsteady front advances along the wide side of the annulus faster than along the narrow side. At sufficiently long times the interface becomes pseudo-parallel to the annulus axis due to the large aspect ratio, as we can see in Fig. 3.

If the fluid streams remain distinct, such displacements will only be partially complete after pumping one annular volume.[2] However, it is not clear that the fluid streams will remain distinct. Tehrani et al. report observing interfacial instabilities on the narrow side of the annulus in some situations where a narrow side channel emerged, [13,14]. We have also observed similar instabilities in some of our preliminary experiments, an example of which we show in Fig. 4.

If these interfacial instabilities lead to azimuthal mixing around the annulus, then the displacement may still be effective from an industrial perspective. In place of the predicted unsteady fingering, we will have azimuthal mixing and axial dispersion of the mixed region, which may grow at an acceptably slow rate, e.g. $\sim t^{1/2}$ rather than $\sim t$. Thus, the study of interfacial instabilities in parallel two-layer annular Hele-Shaw flows is a problem of practical interest. This is the subject of this paper.

The objective of this paper is to predict the onset of interfacial instabilities in two-layer flows parallel to the axis of a narrow eccentric annulus. We start in this paper by focussing on the case of two Newtonian fluids of different densities and viscosities, flowing in parallel along a uniform narrow eccentric annulus at constant inclination to vertical. In reality, an oil or gas well extends hundreds or thousands of metres and may exhibit slow variations in

[2] Large excess volumes are not pumped as it can be a problem to dispose of excess fluids at the wellhead.

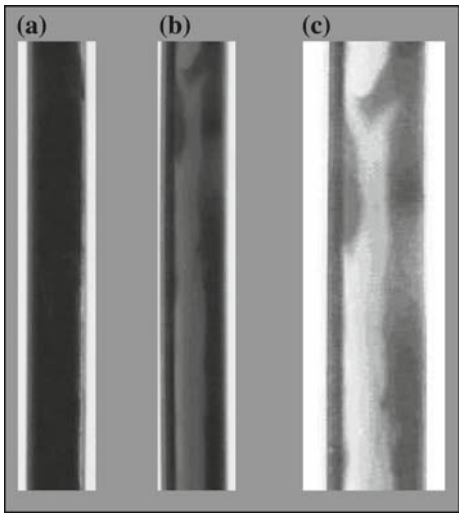

Fig. 4 Example interfacial instability from the 2 m UBC displacement rig: (**a**) side view of annulus, with narrow side to right, wide side to left; (**b**) narrow side view of annulus showing "mud" channel; (**c**) detail of instability on narrow side. Dark colour is the displacing fluid and light colour the displaced fluid. See also Tehrani et al. [13,14]

inclination, casing eccentricity and hole diameter along the length. A sequence of fluids are pumped around the flow path at varying flow rates. The fluids themselves are non-Newtonian, typically both shear-thinning and with a yield stress. All of this leads to a problem that is too complicated to be able to analyse and extract physically meaningful results, and hence our initial simplifications. In a second companion paper we consider shear-thinning and yield-stress effects.

The flows we consider are unsteady parallel two-layer flows in an (eccentric annular) Hele-Shaw cell. Due to the analogy with porous-media Darcy flows and the importance of such flows in the petroleum industry and in water management, there is an extensive literature covering this type of flow. In so far as flow instabilities are concerned, viscous fingering of planar displacement fronts is perhaps the most commonly studied area. The reader may consult [15] for a review of such instabilities,[3] which are not directly relevant here.

Parallel-flow instabilities are far less studied. The earliest such study is that of Raghavan and Marsden [16], who showed that in the presence of a density difference, if the heavier fluid is on top of the lighter fluid, the flow is unstable for all viscosity ratios. If instead the lighter fluid is on top of the heavier fluid the flow will be unstable only for large viscosity ratios and where the more viscous is on top of the less viscous. The iso-density case results in stability, or neutral stability in the absence of surface tension.

This iso-density case was studied further by Zeybek and Yortsos [17,18], both experimentally and theoretically. They considered the parallel flow of two immiscible fluids in a Hele-Shaw cell. Extension of the linear analysis to a weakly nonlinear analysis revealed the presence of solitary wave solutions at the interface in the long-wavelength limit. Although the fluids are immiscible, capillary effects enter the analysis only at high order in the wavenumber α, and thus are neglected for the long-wavelength limit. Equivalently, one could consider the miscible limit of infinite capillary number and the results would be the same, except resulting in neutral stability for the linear analysis. Experimentally, Zeybek and Yortsos showed that after the solitons leave the channel the interface remains flat. More recently, this type of study has been extended to ferro-fluids, where a magnetic field is used to stabilize or destabilize the interface [19].

The analyses above are based on the steady Darcy law, which means that time-dependent effects enter the stability problem only via the kinematic condition. It is not clear that this procedure is correct for the study of instability in

[3] The interested reader may also find a bibliography of over 500 papers, books and articles can be found at: http://www.maths.ox.ac.uk/∼howison/Hele-Shaw/

parallel Hele-Shaw flows. In the usual derivation of the Hele-Shaw approximation, one neglects both the nonlinear inertial and the linear acceleration terms, under the assumption that the reduced Reynolds number is small. Neglect of the nonlinear terms is justified by a scaling argument, but neglect of the accelerations is only justified by an additional argument that the appropriate timescale for changes in velocity is the convective timescale.

In the case where there are changes in the velocity field that are not driven by advection, these terms may be retained while the nonlinear terms are neglected. In viscous flows such changes are usually driven by boundary effects, e.g. classical studies of start-up flows do not involve inertia. It is also reasonable to suppose that interfacial instability may initiate a flow that evolves on a timescale that is different to the advective timescale. It is for this reason that in our analysis the acceleration terms are retained in the Darcy law. Of course, once an instability saturates the flow is likely to lose its planar orientation and the scaling argument that permitted neglect of the nonlinear inertial terms become invalid.

Inclusion of the inertial and acceleration terms in a parallel Hele-Shaw flow has been considered by Gondret et al. [20,21], who derive dispersion relations that may be considered as either the extension of the classical Kelvin–Helmholtz results or as an extension of the parallel Darcy-flow results. This theory has been applied primarily to gas–liquid flows, with stable density orientation, where it has reasonable predictive validity. More recent experimental, computational and analytical treatments can be found in [22–26], again all for gas–liquid flows.

Although it would be possible to include inertial terms in our analysis below, we have not done so. There are already a number of additional difficulties and differences to the existing work. First, we consider only liquid–liquid flows and in a sequel (part 2) to our paper we will consider yield stress and shear-thinning effects. Second, oil and gas wells can be inclined at all angles. Axial buoyancy gradients influence the base flow and azimuthal buoyancy gradients enter into the jump conditions. Thus, we can not consider only horizontal or vertical Hele-Shaw cells. Thirdly, the geometry of the eccentric annulus enters both in the definition of the base flow and directly into the stability problem. Additionally, this geometry means that the domain is finite, which hampers analytical progress.

A plan of our paper is as follows. In Sect. 2 following, we summarize the main points of the general annular displacement model derived in [4,11,12], and simplify this model to the case of two Newtonian fluids. In Sect. 3 we formulate the stability problem for parallel two-layer base flows. Section 4 focuses on the case of a concentric annulus, where we are able to solve the stability problem analytically. Eccentric annuli are considered in Sect. 5. Computational solutions of the eigenvalue problems are used and also the long-wavelength limit is analysed. The paper closes with a brief discussion in Sect. 6.

2 Eccentric annular displacement flows

In [12] the primary-cementing process has been modelled by the following evolution PDE:

$$\nabla \cdot \left[\frac{\rho}{H} \nabla \Psi_t \right] = -\nabla \cdot [\mathbf{S} + \mathbf{f}], \tag{1}$$

where in general

$$\mathbf{S} = \left(\frac{\chi(|\nabla \Psi|) + \tau_Y / H}{|\nabla \Psi|} \right) \nabla \Psi \Leftrightarrow |\mathbf{S}| > \tau_Y / H, \tag{2}$$

$$|\nabla \Psi| = 0 \Leftrightarrow |\mathbf{S}| \leq \tau_Y / H. \tag{3}$$

Here ρ is the fluid density, Ψ is the stream function, the *unwrapped* narrow annular space is $(\phi, \xi) \in (0, 1) \times (0, Z)$, the annular gap half-width is $H(\phi) = 1 + e \cos \pi \phi$, and $e \in [0, 1)$ is the eccentricity; see Fig. 1. The vectorfield $\mathbf{S}$ represents the modified pressure gradient field, due to the flux $|\nabla \Psi|$ of the fluid through a channel of half-width H. The function χ is a positive increasing function of $|\nabla \Psi|$, which represents the purely viscous part of the frictional pressure gradient. The exact form of χ depends on H, and on the rheological parameters that characterize the fluid. The fluid yield stress is denoted τ_Y and the vector field $\mathbf{f}$ represents the gravitational force:

$$\mathbf{f} = \left(\rho \frac{\cos \beta}{\mathrm{St}^*}, \rho \frac{\sin \beta \sin \pi \phi}{\mathrm{St}^*} \right). \tag{4}$$

Here β is the angle of inclination of the annulus from vertical and St* is the Stokes number, which represents the balance between static pressure and viscous stress gradients. These parameters are discussed further Sect. 3.3.

The density and all the rheological properties of the fluids may depend on the mixture concentration, which in the case of two fluids can be characterized by the concentration of fluid 1, say $\bar{c}(\phi, \xi, t)$. In [4] the concentration is simply advected along the annulus:

$$\frac{1}{\epsilon}\frac{\partial}{\partial t}\left[H\overline{c}\right] + \frac{\partial}{\partial \phi}\left[H\overline{v}\,\overline{c}\right] + \frac{\partial}{\partial \xi}\left[H\overline{w}\,\overline{c}\right] = 0, \tag{5}$$

where ϵ denotes the ratio of viscous and advective timescales, and where the gap-averaged velocities are defined in terms of the stream function by:

$$\overline{v} = -\frac{1}{H}\frac{\partial \Psi}{\partial \xi}, \qquad \overline{w} = \frac{1}{H}\frac{\partial \Psi}{\partial \phi}. \tag{6}$$

Henceforth we shall concentrate on the case where we have only two fluids and both are Newtonian.

2.1 Displacements flows of two Newtonian fluids

When the concentration is simply advected by the velocity field, we have a miscible fluid that does not mix in the timescale of interest, i.e., this is the high-Péclet-number limit of a miscible displacement. As there is no mixing, we may equivalently track any of the iso-concentration curves as the interface and advect this "level set" via a kinematic equation; see [11] for further details of this equivalency. Thus we assume that our domain Ω is divided into Ω_1 and Ω_2 by a smooth curve C, defined by:

$$F(\phi, \xi, t) = 0. \tag{7}$$

The function $F(\phi, \xi, t)$ satisfies the gap-averaged kinematic equation:

$$\frac{H}{\epsilon}\frac{\partial F}{\partial t} - \frac{\partial \Psi}{\partial \xi}\frac{\partial F}{\partial \phi} + \frac{\partial \Psi}{\partial \phi}\frac{\partial F}{\partial \xi} = 0. \tag{8}$$

Now because the fluid properties are constant in each domain, we have that $\nabla \cdot \mathbf{f} = 0$. As the fluids are Newtonian, $\tau_Y = 0$. By averaging across the annular gap we find that

$$\chi(|\nabla \Psi|) = \frac{3\kappa|\nabla \Psi|}{H^3}, \qquad \mathbf{S} = \frac{3\kappa}{H^3}\nabla \Psi, \tag{9}$$

which should be familiar from classical Hele-Shaw flows. Hence in each fluid domain we have:

$$\rho_k \nabla \cdot \left[\frac{\nabla \Psi_t}{H}\right] + \nabla \cdot \mathbf{S}_k = 0, \qquad (\phi, \xi) \in \Omega_k,\ k = 1, 2, \tag{10}$$

where the index k is used to denote the fluid. Equation 10 is supplemented with the following boundary conditions:

$$\Psi(0, \xi, t) = 0. \tag{11}$$

$$\Psi(1, \xi, t) = Q(t), \tag{12}$$

on the wide ($\phi = 0$) and narrow ($\phi = 1$) sides of the annulus, respectively. Here $Q(t)$ represents the total flow rate through the annulus, appropriately scaled. At the interface the following two jump/continuity conditions are satisfied,

$$\Psi|_1^2 = 0, \tag{13}$$

$$\left[\left(\frac{\rho_k \cos\beta}{\mathrm{St}^*}, \frac{\rho_k \sin\beta \sin\pi\phi}{\mathrm{St}^*}\right) + \frac{\rho_k}{H}\nabla \Psi_t + \mathbf{S}_k\right] \cdot \nabla F|_1^2 = 0. \tag{14}$$

The first of these is simply continuity of Ψ, i.e., of the normal velocity, whereas (14) defines the jump in normal derivative of Ψ. Condition (14) comes from continuity of the pressure; see [12].

So far all our equations and variables have been presented in dimensionless form, as this will be used for the analysis throughout the paper. In Sect. 3.3 we define the relevant dimensionless parameters of the problem in terms of the dimensional process parameters. Throughout the paper we shall denote dimensional quantities with a "hat" symbol, (e.g., later $\hat{g}$ denotes the gravitational acceleration), and dimensionless quantities will not have the "hat". The model described above is explained in more detail in [12], and the reader interested in the physical derivation is also referred to [4,7] where a pseudo-steady version is treated.

3 Stability of two-layer flows

As discussed in Sect. 1, under various conditions the interface between fluids is known to elongate into a long finger, advancing up the wide side of the annulus ahead of the mean flow. At longer times, due to the large aspect ratio of the well, these unsteady flows closely resemble a parallel two-layer. It is such flows that we study here.

We shall assume an infinitely long uniform annulus, with fluid 1 on the wide side of the annulus and fluid 2 on the narrow side. The interface is defined by, $F = \phi - \phi_i(\xi, t) = 0$. Our system of equations may be summarized as follows:

$$\nabla \cdot \left[\mathbf{S}_k + \frac{\rho_k}{H}\nabla\Psi_{k,t}\right] = 0, \quad \text{in } \Omega_k, \tag{15}$$

$$\Psi_1(0, \xi, t) = 0, \tag{16}$$

$$\Psi_2(1, \xi, t) = 1, \tag{17}$$

and at $\phi = \phi_i(\xi, t)$,

$$\frac{H}{\epsilon}\frac{\partial\phi_i}{\partial t} + \frac{\partial\Psi_k}{\partial\xi} + \frac{\partial\Psi_k}{\partial\phi}\frac{\partial\phi_i}{\partial\xi} = 0, \quad \text{at } \phi = \phi_i(\xi, t) \tag{18}$$

$$\Psi_k|_{k=1}^{k=2} = 0, \tag{19}$$

$$\left(\mathbf{S}_k + \frac{\rho_k}{H}\nabla\Psi_{k,t}\right)\cdot\mathbf{n}\Big|_{k=1}^{k=2} = -b^*(\cos\beta, \sin\beta\sin\pi\phi_i)\cdot\mathbf{n}, \tag{20}$$

with buoyancy parameter $b^* = [\rho_2 - \rho_1]/\mathrm{St}^*$, and

$$\mathbf{S}_k = \frac{3\kappa_k}{H^3}\nabla\Psi_k.$$

3.1 Basic flow

The system (15)–(20) has a one-dimensional steady solution, that we denote by $\Psi_{1,0}(\phi)$ and $\Psi_{2,0}(\phi)$, in fluids 1 and 2, respectively:

$$\Psi_{1,0}(\phi) = C_1 P(\phi, e) \tag{21}$$

$$\Psi_{2,0}(\phi) = 1 + C_2[P(\phi, e) - P(1, e)], \tag{22}$$

where $P(\phi, e)$ is the following cubic function of the eccentricity, e:

$$P(\phi, e) = \pi\phi + 3e\sin\pi\phi + \frac{3e^2}{2}[\pi\phi + \cos\pi\phi\sin\pi\phi] + \frac{e^3}{3}[\cos^2\pi\phi\sin\pi\phi + 2\sin^3\pi\phi] = \pi\int_0^\phi H^3(\tilde{\phi})\,\mathrm{d}\tilde{\phi} \tag{23}$$

The constants C_1 and C_2 are defined by:

$$C_1 = \frac{\frac{1}{3\pi}\frac{b}{\kappa_2}[P(\phi_{i,0}, e) - P(1, e)] - 1}{\frac{\kappa_1}{\kappa_2}[P(\phi_{i,0}, e) - P(1, e)] - P(\phi_{i,0}, e)}$$

$$C_2 = \frac{\frac{1}{3\pi}\frac{b}{\kappa_2}P(\phi_{i,0}, e) - \frac{\kappa_1}{\kappa_2}}{\frac{\kappa_1}{\kappa_2}[P(\phi_{i,0}, e) - P(1, e)] - P(\phi_{i,0}, e)}$$

where b is the axial buoyancy parameter:

$$b = b^* \cos\beta.$$

We note that the basic solutions are defined by a minimal set of four dimensionless parameters: $\phi_{i,0}, e, b/\kappa_2, \kappa_1/\kappa_2$.

3.2 Temporal stability problem

We consider the stability of linear perturbation of the basic flows, by assuming an expansion of form:

$$\Psi_k = \Psi_{k,0} + \delta\Psi_{k,1} + \delta^2\Psi_{k,2} + \cdots,$$
$$\mathbf{S}_k = (S_{k,\phi,0}, 0) + \delta\mathbf{S}_{k,1} + \delta^2\mathbf{S}_{k,2} + \cdots$$
$$\phi_i = \phi_{i,0} + \delta h + \cdots,$$

for $\delta \ll 1$. We substitute these expressions in (15)–(20), expand with respect to δ, and retain only the terms linear in δ. The linear stability problem for $\Psi_{k,1}$ and h is as follows:

$$\nabla \cdot \left[\mathbf{S}_{k,1} + \frac{\rho_k}{H}\nabla\Psi_{k,1,t}\right] = 0, \quad \text{in } \Omega_k, \tag{24}$$
$$\Psi_{1,1}(0, \xi, t) = 0, \tag{25}$$
$$\Psi_{2,1}(1, \xi, t) = 0. \tag{26}$$

The interfacial conditions are linearized onto the zeroth-order interface position, $\phi = \phi_{i,0}$:

$$\frac{H}{\epsilon}h_t + \Psi_{k,1,\xi} + \Psi_{k,0,\phi}h_\xi = 0, \tag{27}$$
$$(\Psi_{k,1} + h\Psi_{k,0,\phi})\big|_{k=1}^{k=2} = 0, \tag{28}$$
$$\left(S_{k,1,\phi} + \frac{\rho_k}{H}\Psi_{k,1,\phi t}\right)\Big|_{k=1}^{k=2} = bh_\xi \tan\beta \sin\pi\phi_{i,0}, \tag{29}$$

with $\mathbf{S}_{k,1}$ defined by

$$\mathbf{S}_{k,1} = \frac{3\kappa_k}{H^3}\nabla \cdot \Psi_{k,1}.$$

We proceed in the usual way via a normal mode expansion of the linear perturbation:

$$\Psi_{1,k} \sim f_k(\phi)\mathrm{e}^{\mathrm{i}(\alpha\xi - st)}, \qquad h \sim h_0\mathrm{e}^{\mathrm{i}(\alpha\xi - st)},$$

which we substitute in (24)–(29) to give:

$$\mathrm{i}s\rho_1\left(D\left(\frac{D}{H}\right) - \frac{\alpha^2}{H}\right)f_1 = 3\kappa_1\left(D\left(\frac{D}{H^3}\right) - \frac{\alpha^2}{H^3}\right)f_1 \quad \phi \in (0, \phi_{i,0}), \tag{30}$$

$$\mathrm{i}s\rho_2\left(D\left(\frac{D}{H}\right) - \frac{\alpha^2}{H}\right)f_2 = 3\kappa_2\left(D\left(\frac{D}{H^3}\right) - \frac{\alpha^2}{H^3}\right)f_2 \quad \phi \in (\phi_{i,0}, 1), \tag{31}$$
$$f_1(0) = 0, \tag{32}$$
$$f_2(1) = 0, \tag{33}$$

where $D = \frac{\mathrm{d}}{\mathrm{d}\phi}$. At $\phi = \phi_{i,0}$, we have the conditions:

$$-\frac{H}{\epsilon} s h_0 + \alpha(f_k + \Psi_{k,0,\phi} h_0) = 0, \tag{34}$$

$$(h_0 \Psi_{0,k,\phi} + f_k)|_1^2 = 0, \tag{35}$$

$$\left[\left(\frac{3\kappa_k}{H^3} - \mathrm{i}s\frac{\rho_k}{H}\right) D f_k\right]\Big|_{k=1}^{k=2} = \mathrm{i}\alpha b h_0 \tan\beta \sin\pi\phi_{i,0}. \tag{36}$$

3.3 Dimensionless parameters and simplifications

The Stokes number St^* is defined by

$$\mathrm{St}^* = \frac{\hat{\kappa}^* \hat{w}^*}{\hat{\rho}^* \hat{g} \hat{d}^2}, \tag{37}$$

where $\hat{\kappa}^*$ is the maximum of the dimensional viscosities (recall our convention of denoting dimensional quantities with the $\hat{\cdot}$ symbol). Similarly, $\hat{\rho}^*$ is the maximum of the two-dimensional fluid densities. Note that $\hat{\kappa}^*$ and $\hat{\rho}^*$ are used as scales for the dimensionless viscosities and densities. In (37) $\hat{d}$ is the difference between outer and inner radii of the annulus, and $\hat{w}^*$ denotes the mean axial velocity of the flow. The Stokes number does not appear explicitly in either the computation of the base flow, nor in the stability problem, as it is modulated by the density difference and enters into the parameter b.

We have seen that the base flow depends on only the four parameters: $\phi_{i,0}$, e, b/κ_2, κ_1/κ_2. At first appearances the stability problem is far more complex. However, on dividing through (30) by κ_1, (31) by κ_2, and (36) by κ_2 we see that only ρ_1/κ_1, ρ_2/κ_2, ϵ and β remain, to be added to the four parameters of the basic flow. On more careful inspection, we see that if we consider s/ϵ as our eigenvalue, then the eigenvalue problem for s/ϵ may be expressed in terms of $\phi_{i,0}$, e, b/κ_2, κ_1/κ_2, $\epsilon\rho_1/\kappa_1$, $\epsilon\rho_2/\kappa_2$ and β. It is of interest to understand clearly, in physical dimensional terms, what the seven parameters are.

First of all, the parameter ϵ is simply the ratio of viscous to advective timescales. Thus, by considering s/ϵ as our eigenvalue, amounts to considering growth rates in terms of the advective timescale rather than the viscous timescale. Although the growth rates are scaled in this way, the marginal stability conditions computed are identical.

In Fig. 5 we show schematically the physical positions of the fluids and interface in the annulus for the two-layer flows we consider. The interface position, $\phi_{i,0}$, eccentricity e, inclination β, and viscosity ratio κ_1/κ_2, need no explanation. The ratio b/κ_2 in dimensional variables is given by:

$$\frac{b}{\kappa_2} = \frac{[\hat{\rho}_2 - \hat{\rho}_1]\hat{g}\hat{d}^2 \cos\beta}{\hat{\kappa}_2 \hat{w}^*}.$$

Therefore, we can see that b/κ_2 is a balance between the axial buoyancy stress and the viscous stress in fluid 2.

Although b/κ_2 appears in the problem for the basic flow, in the stability problem β and b only appear directly in the combination: $b\tan\beta\sin\pi\phi_{i,0}$. This quantity is in fact the azimuthal component of the buoyancy force, $[\hat{\rho}_2 - \hat{\rho}_1]\hat{g}\sin\beta\sin\pi\phi_{i,0}$, that acts across the interface; see Fig. 5. From the position of the fluids, (i.e., fluid 2 is on the lower side of the annulus), we might expect that $b > 0$ will give a stabilizing effect and $b < 0$ will be destabilizing. We will see below that this is true. In general it is more convenient to work with b^* than b, especially when considering horizontal wells, $\beta \to \pi/2$, as the term $b\tan\beta$ ($=b^*\sin\beta$) appears in the jump conditions.

The parameter $\epsilon\rho_k/\kappa_k$ is defined by:

$$\frac{\epsilon\rho_k}{\kappa_k} = \frac{\hat{\rho}_k \hat{w}^* \hat{d}^2}{\pi \hat{r}_a \hat{\kappa}_k}, \tag{38}$$

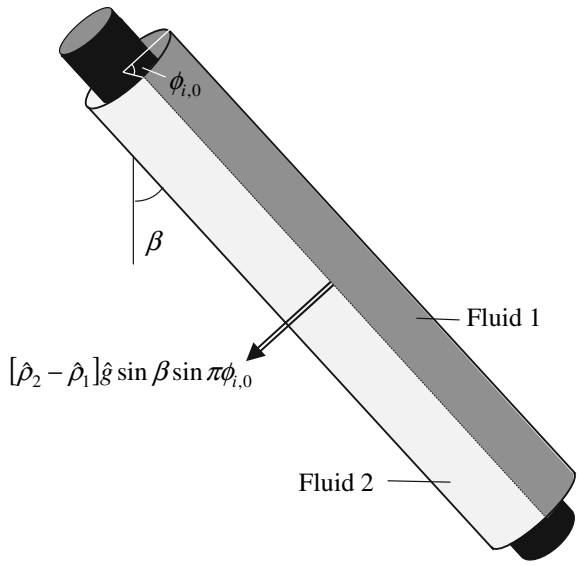

Fig. 5 Schematic of interface and fluid positions in the two-layer flows considered

where $\hat{r}_a$ is the mean radius of the annulus. The aspect ratio of the mean annular gap to mean annular circumference is:

$$\hat{d}/(\pi\hat{r}_a) \ll 1,$$

i.e., we consider that the annulus is narrow. Thus, the parameter $\epsilon\rho_k/\kappa_k$ is the product of the aspect ratio with a Reynolds number of fluid k, based on mean annular half-gap width and the mean velocity $\hat{w}^*$. This product is identifiable as the *reduced* Reynolds number that is commonly found in lubrication and thin-film problems. Accordingly, we denote

$$\frac{\epsilon\rho_k}{\kappa_k} = \mathrm{Re}_k. \tag{39}$$

Since the model we analyse is a Hele-Shaw model in which the nonlinear inertial terms have been neglected, implicitly we should have $\mathrm{Re}_k \lesssim 1$ in each fluid. Later we will see that the difference in reduced Reynolds numbers is one governing parameter in determining the stability of the flow. As we may see from (38), this difference arises only from a difference in the kinematic viscosity of the fluids: $\hat{\kappa}_k/\hat{\rho}_k$.

3.4 Single-fluid stability

In general, it is necessary to solve the eigenvalue problem (30)–(36) computationally. However, there are some simplified situations that permit analysis and which give us some insight. We commence with the flow of a single fluid along the annulus, and consider a normal mode perturbation

$$\Psi_1 \sim f(\phi)\mathrm{e}^{\mathrm{i}(\alpha\xi - st)}.$$

The field equation for f is

$$\mathrm{i}\frac{s}{\epsilon}\frac{\mathrm{Re}}{3}\left(D\left(\frac{D}{H}\right) - \frac{\alpha^2}{H}\right)f = \left(D\left(\frac{D}{H^3}\right) - \frac{\alpha^2}{H^3}\right)f. \tag{40}$$

Multiplying (40) by f^*, the complex conjugate of f, and integrating (by parts) with respect to ϕ, we obtain:

$$\mathrm{i}\frac{s}{\epsilon}\frac{\mathrm{Re}}{3} = \frac{\int_0^1 \frac{|Df|^2}{H^3}\,\mathrm{d}\phi + \alpha^2 \int_0^1 \frac{|f|^2}{H^3}\,\mathrm{d}\phi}{\int_0^1 \frac{|Df|^2}{H}\,\mathrm{d}\phi + \alpha^2 \int_0^1 \frac{|f|^2}{H}\,\mathrm{d}\phi} \tag{41}$$

All the functionals on the right-hand side of (41) are real positive definite. As α is real, it follows that s is pure imaginary, $s = \mathrm{i}s_I$, and the growth rate $s_I < 0$. Thus, the single fluid flow is always linearly stable. Temporal instability can only occur for the two-fluid problem.

This result is wholly intuitive as the base transient Hele-Shaw model for a single fluid has only accelerations and viscous dissipation. Thus, there is not the usual mechanism to transfer energy from the base flow to the perturbation, via inertia. In fact, the base flow does not appear in the linear stability problem. For the two-fluid problem, both the base flow and buoyancy forces appear directly in the jump conditions at the interface.

3.5 Non-trivial perturbations of the two-fluid problem

Turning to the two-fluid problems, we note that in order to find an unstable mode it suffices to consider only cases where both $h_0 \neq 0$ and $\alpha \neq 0$. For $h_0 = 0$ the jump conditions (47) and (48) become homogeneous. Thus, following the procedure in Sect. 3.4 above, we may multiply by f_k^*, integrate across each fluid layer, sum the resulting expressions and show that $s_I < 0$. The interfacial terms in these integrations by parts will cancel using (47) and (48). Again this result is not surprising, as without allowing an interfacial perturbation there is no mechanism for the base flow to transfer energy to the perturbation.

If $\alpha = 0$ then (46) implies either $s = 0$, in which case the perturbation is neutrally stable, or instead $h_0 = 0$. Although the case $\alpha = 0$ gives only a neutrally stable perturbation, the long-wavelength limit, $\alpha \ll 1$, does give non-trivial perturbations which we study in Sect. 5.2.

Hereafter we consider only non-trivial perturbations, i.e., those that may potentially become unstable. We thus assume that $h_0 \neq 0$, and rescale f_k by dividing through with $h_0 H(\phi_{i,0})$, (retaining the same notation for simplicity); (30)–(36) become:

$$\mathrm{i}\frac{s}{\epsilon}\frac{\mathrm{Re}_1}{3}\left(D\left(\frac{D}{H}\right) - \frac{\alpha^2}{H}\right) f_1 = \left(D\left(\frac{D}{H^3}\right) - \frac{\alpha^2}{H^3}\right) f_1 \quad \phi \in (0, \phi_{i,0}) \tag{42}$$

$$\mathrm{i}\frac{s}{\epsilon}\frac{\mathrm{Re}_2}{3}\left(D\left(\frac{D}{H}\right) - \frac{\alpha^2}{H}\right) f_2 = \left(D\left(\frac{D}{H^3}\right) - \frac{\alpha^2}{H^3}\right) f_2 \quad \phi \in (\phi_{i,0}, 1) \tag{43}$$

$$f_1(0) = 0, \tag{44}$$

$$f_2(1) = 0. \tag{45}$$

At $\phi = \phi_{i,0}$, we have the conditions:

$$\alpha(f_k + W_{i,k}) = \frac{s}{\epsilon}, \tag{46}$$

$$(f_k + W_{i,k})|_1^2 = 0, \tag{47}$$

$$\left(\frac{1}{H^2} - \mathrm{i}\frac{s}{\epsilon}\frac{\mathrm{Re}_2}{3}\right) Df_2 = \frac{\kappa_1}{\kappa_2}\left(\frac{1}{H^2} - \mathrm{i}\frac{s}{\epsilon}\frac{\mathrm{Re}_1}{3}\right) Df_1 + \mathrm{i}\frac{\alpha b^* \sin\beta \sin\pi\phi_{i,0}}{3\kappa_2}, \tag{48}$$

where $W_{i,k}$ is the interfacial velocity of the basic flow in fluid k, i.e.

$$W_{i,k} = \frac{1}{H(\phi_{i,0})}\frac{\mathrm{d}}{\mathrm{d}\phi}\Psi_{0,k}(\phi_{i,0}).$$

We study (42)–(48) for the remainder of our paper.

3.5.1 The viscous limit

Suppose now that we consider s/ϵ fixed, and consider the limit $\epsilon \to 0$. In this limit the reduced Reynolds numbers $\epsilon\rho_k/\kappa_k \to 0$ and the fluid accelerations become negligible. We are left with the following stability problem:

$$H^3 D\left(\frac{Df_k}{H^3}\right) - \alpha^2 f_k = 0,$$

in each fluid layer, with boundary conditions (44) and (45), interfacial conditions (46), (47), and with (48) replaced with

$$Df_2 = \frac{\kappa_1}{\kappa_2} Df_1 + \mathrm{i}\frac{\alpha b^* \sin\beta \sin\pi\phi_{i,0} H^2}{3\kappa_2}. \tag{49}$$

This problem is the stability problem that arises from considering the steady Hele-Shaw model in [4–7], i.e., the viscous limit of the model considered here.

If the azimuthal buoyancy force term, $b^* \sin\beta \sin\pi\phi_{i,0}$, is zero we may show that f_k is real and also that s/ϵ is real. This leads to a neutrally stable mode that is purely advected with the interface. This is one of the reasons for including the acceleration terms in our study of flow stability, i.e., we expect that in the absence of buoyancy effects, viscosity difference should still have an effect on the flow stability.

Let us suppose instead that $b^* \sin\beta \sin\pi\phi_{i,0} \neq 0$. We may then manipulate the eigenproblem to give:

$$\frac{s_I}{\epsilon}\frac{b^* \sin\beta \sin\pi\phi_{i,0}}{3\kappa_2 H} = \frac{(W_{i,2} - W_{i,1}) f_{1,R} f_{2,R} (L_1 - L_2)}{(|f_1|^2 + |f_2|^2) f_{1,R} - |f_1|^2 (W_{i,2} - W_{i,1})} - (L_1 + L_2), \tag{50}$$

where the terms $f_k(\phi)$ and $H(\phi)$ are evaluated at the interface, $\phi = \phi_{i,0}$, and where

$$L_1(\phi_{i,0}) = \frac{\kappa_1}{\kappa_2}\int_0^{\phi_{i,0}} \frac{|Df_1|^2 + \alpha^2 |f_1|^2}{H^3(\phi)} \mathrm{d}\phi,$$
$$L_2(\phi_{i,0}) = \int_{\phi_{i,0}}^1 \frac{|Df_2|^2 + \alpha^2 |f_2|^2}{H^3(\phi)} \mathrm{d}\phi.$$

We see that the functionals $L_1(\phi_{i,0})$ and $L_2(\phi_{i,0})$, which are positive definite, correspond to energy dissipation via viscosity in the two fluid layers. Thus the last term on the right-hand side of (50) is negative. Assuming that $b^* \sin\beta \sin\pi\phi_{i,0} > 0$, i.e., fluid 2 is heavier, then the dissipation has a stabilizing effect; see Fig. 5. The first term in (50) less easy to understand, but we can see that both a difference in dissipation functionals and interfacial velocity is involved. This term vanishes when the interfacial velocity difference is zero, but otherwise we cannot determine the sign.

Note that if $b^* \sin\beta \sin\pi\phi_{i,0} < 0$, then the dissipative terms are destabilizing. Our interpretation of this is that even though we may see from the configuration in Fig. 5 that this situation would be mechanically unstable, in the context of this model we have only viscous terms to transfer energy to the perturbation (i.e., no acceleration terms). Since the second term in (50) is of indeterminate sign, it is very likely that flows with $b^* \sin\beta \sin\pi\phi_{i,0} < 0$ are unstable for some range of $\phi_{i,0}$.

4 Concentric annuli, $e = 0$

In the case of a concentric annulus ($H(\phi) = 1$), (42) and (43) become

$$\left(1 - \mathrm{i}\frac{s}{\epsilon}\frac{\mathrm{Re}_1}{3}\right)(D^2 - \alpha^2) f_1 = 0, \quad \phi \in (0, \phi_{i,0})$$
$$\left(1 - \mathrm{i}\frac{s}{\epsilon}\frac{\mathrm{Re}_2}{3}\right)(D^2 - \alpha^2) f_2 = 0, \quad \phi \in (\phi_{i,0}, 1)$$

We note that if $\left(1 - \mathrm{i}\frac{s}{\epsilon}\frac{\mathrm{Re}_k}{3}\right) = 0$, then $s_I < 0$ and these modes are stable. Therefore, for instability we may assume that $\left(1 - \mathrm{i}\frac{s}{\epsilon}\frac{\mathrm{Re}_k}{3}\right) \neq 0$, and cancel this term. It is interesting to observe that the eigenvalue s/ϵ does not now appear in the field equations, but only the jump conditions. This degeneracy is peculiar to the case of two Newtonian fluids. The solutions that satisfy (44) and (45) are:

$$f_1(\phi) = A_1 \sinh \alpha\phi, \qquad f_2(\phi) = A_2 \sinh \alpha(\phi - 1), \tag{51}$$

for constants A_1 and A_2.

For concentric annuli the expressions for the basic flow simplify considerably. The axial velocities are constant across each fluid layer, with a jump at the interface:

$$W_{i,1} = \frac{1 + (1-\phi_{i,0})\frac{b}{3\kappa_2}}{\phi_{i,0} + (1-\phi_{i,0})\frac{\kappa_1}{\kappa_2}}, \qquad W_{i,2} = \frac{\frac{\kappa_1}{\kappa_2} - \phi_{i,0}\frac{b}{3\kappa_2}}{\phi_{i,0} + (1-\phi_{i,0})\frac{\kappa_1}{\kappa_2}}. \tag{52}$$

From (46) and (47) we find

$$A_1 = \frac{1}{\sinh \alpha\phi_{i,0}}\left[\frac{s}{\alpha\epsilon} - \frac{1 + \frac{b}{3\kappa_2}(1-\phi_{i,0})}{\phi_{i,0} + (1-\phi_{i,0})\frac{\kappa_1}{\kappa_2}}\right],$$
$$A_2 = \frac{1}{\sinh \alpha(\phi_{i,0} - 1)}\left[\frac{s}{\alpha\epsilon} - \frac{\frac{\kappa_1}{\kappa_2} + \frac{b}{3\kappa_2}\phi_{i,0}}{\phi_{i,0} + (1-\phi_{i,0})\frac{\kappa_1}{\kappa_2}}\right].$$

Finally, substituting in (48), we find the following quadratic relation for s/ϵ:

$$\begin{aligned} 0 = {} & \frac{\mathrm{i}}{3}\frac{b}{\kappa_2}\alpha \tan\beta \sin\pi\phi_{i,0} + \coth\alpha\phi_{i,0}\left[\frac{s}{\epsilon} - \alpha\frac{1 + \frac{b}{3\kappa_2}(1-\phi_{i,0})}{\phi_{i,0} + (1-\phi_{i,0})\frac{\kappa_1}{\kappa_2}}\right]\frac{\kappa_1}{\kappa_2}\left[1 - \frac{\mathrm{i}\,\mathrm{Re}_1}{3}\frac{s}{\epsilon}\right] \\ & + \coth\alpha(1-\phi_{i,0})\left[\frac{s}{\epsilon} - \alpha\frac{\frac{\kappa_1}{\kappa_2} - \frac{b}{3\kappa_2}\phi_{i,0}}{\phi_{i,0} + (1-\phi_{i,0})\frac{\kappa_1}{\kappa_2}}\right]\left[1 - \frac{\mathrm{i}\,\mathrm{Re}_2}{3}\frac{s}{\epsilon}\right]. \end{aligned} \tag{53}$$

The two roots of (53) give an explicit expression for the growth rates. This expression is algebraically complex and not very enlightening, but the marginal stability condition is useful and can be found easily:

$$\begin{aligned} & \frac{\left[\frac{\kappa_1}{\kappa_2}\left(1 + \frac{b}{3\kappa_2}(1-\phi_{i,0})\right)\coth\alpha\phi_{i,0} + \left(\frac{\kappa_1}{\kappa_2} - \frac{b}{3\kappa_2}\phi_{i,0}\right)\coth\alpha(1-\phi_{i,0})\right]}{\left[\frac{\kappa_1}{\kappa_2}\coth\alpha\phi_{i,0} + \coth\alpha(1-\phi_{i,0})\right]^2} \\ & \times\left(\frac{\alpha\left[\mathrm{Re}_2 - \mathrm{Re}_1\right]\left[\frac{\kappa_1}{\kappa_2} - 1 - \frac{b}{3\kappa_2}\right]}{\left[\phi_{i,0} + (1-\phi_{i,0})\frac{\kappa_1}{\kappa_2}\right]^2}\right) = -\frac{b\tan\beta\sin\pi\phi_{i,0}}{\kappa_2}. \end{aligned}$$

The physical meaning becomes slightly clearer once we substitute for the interfacial velocities. The condition for stability is then that:

$$\frac{b\tan\beta\sin\pi\phi_{i,0}}{\kappa_2} \geq -\frac{\alpha\left[W_{i,1}\frac{\kappa_1}{\kappa_2}\coth\alpha\phi_{i,0} + W_{i,2}\coth\alpha(1-\phi_{i,0})\right]}{\left[\frac{\kappa_1}{\kappa_2}\coth\alpha\phi_{i,0} + \coth\alpha(1-\phi_{i,0})\right]^2} \times \left[\mathrm{Re}_2 - \mathrm{Re}_1\right]\left[W_{i,2} - W_{i,1}\right]. \tag{54}$$

The left-hand side is a measure of the azimuthal buoyancy force, acting across the interface, (see Fig. 5), and is stabilizing when $b > 0$. The terms in the first expression on the right-hand side are a weighted average of the interfacial velocities of the two fluids. If there is only a modest density difference, we would expect that these terms are positive. The denominator is positive definite and therefore, the sign of the product

$$[\mathrm{Re}_2 - \mathrm{Re}_1]\left[W_{i,2} - W_{i,1}\right]$$

determines whether the right-hand side is stabilizing or not. In the event that the fluid densities are identical, we observe that the flows are stable, which follows since the above product becomes proportional to $\left[W_{i,2} - W_{i,1}\right]^2$.

4.1 Typical wavenumber dependence

The least stable eigenmode of the stability problem is that for which the eigenvalue $s = s_R + \mathrm{i}s_I$ is maximal, say $s_{I,\max}$. In Fig. 6 we show some of the typical wavenumber dependence of the least stable eigenvalue, $s_{I,\max}/\epsilon$. At zero wavenumber, see Sect. 3.5, the maximal eigenvalue is zero. As the wavenumber increases, $s_{I,\max}/\epsilon$ changes smoothly and appears to asymptote to a short-wavelength limit as $\alpha \to \infty$. The short-wavelength limits all appear to give $O(1)$ growth or decay rates. In the case that the short-wavelength limit is unstable, this suggests the breakdown of the model since maximal growth is achieved in the limit where the Hele-Shaw approximation becomes invalid. We discuss this further in Sect. 6. For $\beta > 0$, the variation in $s_{I,\max}/\epsilon$ can be non-monotone; see Fig. 6c and d. In Figs. 6a–d we fix the ratio b^*/κ_2, and vary β. For each value of β, we plot $s_{I,\max}/\epsilon$ for four different choices of viscosity ratio, κ_1/κ_2. For the results shown, increasing κ_1/κ_2 appears to destabilize the flow. However, we shall see below that increasing κ_1/κ_2 can also result in increased stability. Thus, it is hard to draw general conclusions.

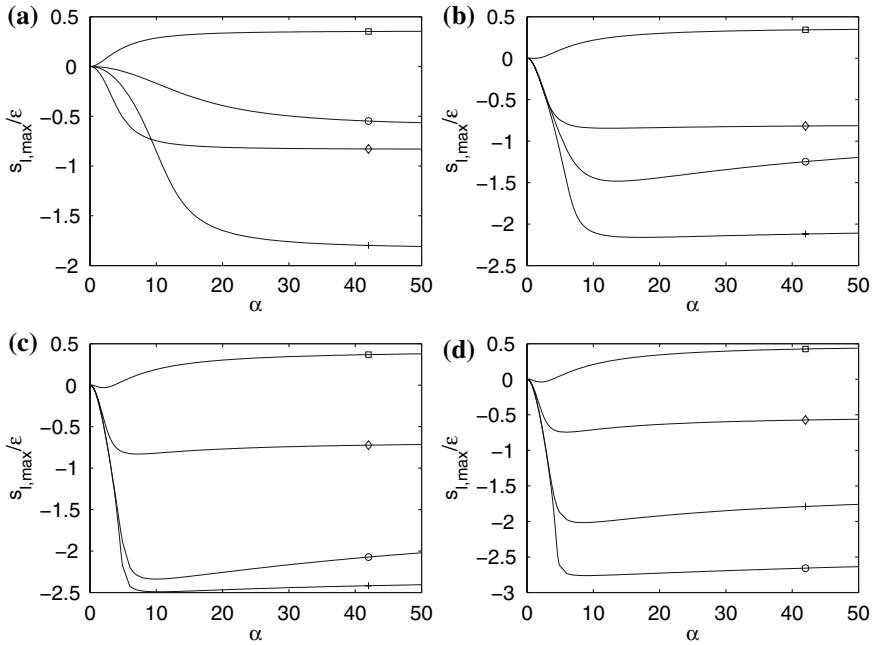

Fig. 6 Examples of typical variations in least stable eigenvalue with wavenumber in a concentric annulus, $e = 0$: $\phi_{i,0} = 0.5$, $b^*/\kappa_2 = 1$, $\epsilon\rho_1/\kappa_1 = 1.0$, $\epsilon\rho_2/\kappa_2 = 0.5$; (**a**) $\beta = 0$; (**b**) $\beta = \pi/6$; (**c**) $\beta = \pi/3$; (**d**) $\beta = \pi/2$. In each figure $\kappa_1/\kappa_2 = 0.02$—marked with o, $\kappa_1/\kappa_2 = 0.1$—marked with +, $\kappa_1/\kappa_2 = 0.5$—marked with $\diamond$, $\kappa_1/\kappa_2 = 2.5$—marked with $\square$

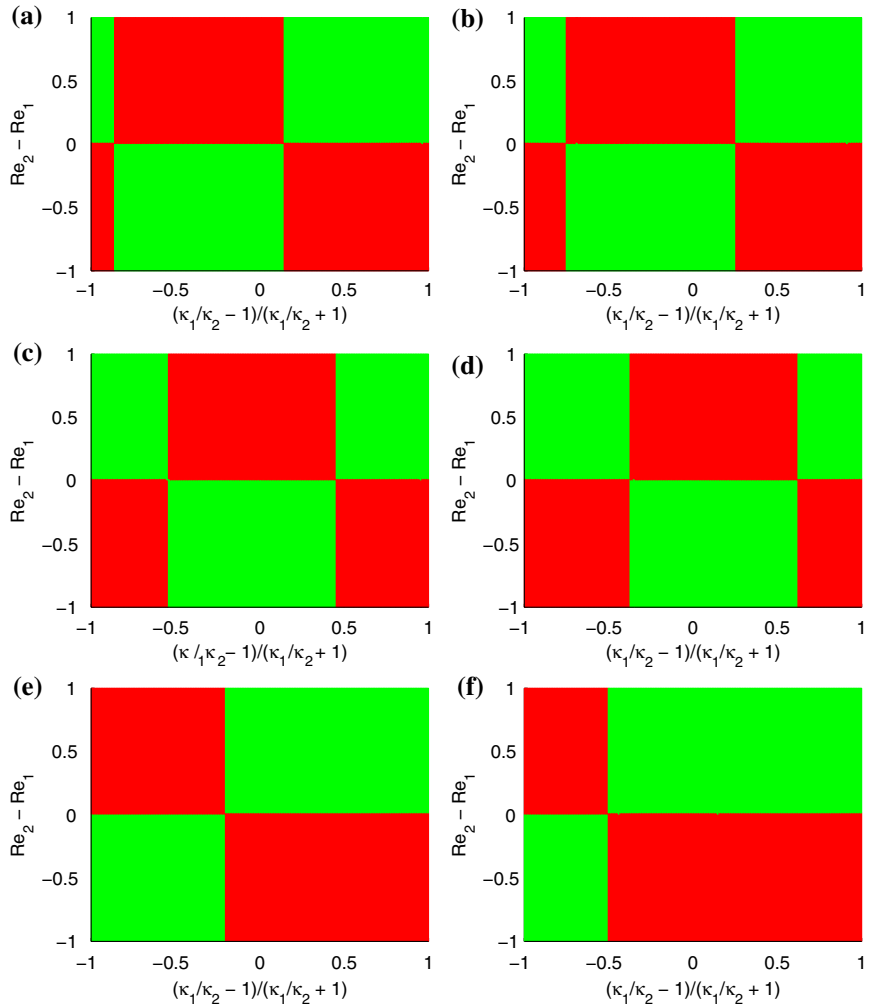

Fig. 7 Regions of marginal stability for a vertical well: $e = 0$, $\beta = 0$, $\phi_{i,0} = 0.5$: (**a**) $b^*/\kappa_2 = 1$; (**b**) $b^*/\kappa_2 = 2$; (**c**) $b^*/\kappa_2 = 5$; (**d**) $b^*/\kappa_2 = 10$; (**e**) $b^*/\kappa_2 = -1$; (**f**) $b^*/\kappa_2 = -2$; unstable—red (dark), stable—green (light)

4.2 Vertical wells

Although the growth rates are of interest, it is perhaps of more interest to simply know whether or not a given flow is stable or unstable. To determine this, we compute the maximum over $\alpha > 0$ of $s_{I,\max}/\epsilon$. We plot below in Fig. 7 regions of stability and instability in the plane (x, y)-plane, where

$$x = \frac{\kappa_1/\kappa_2 - 1}{\kappa_1/\kappa_2 + 1}, \qquad y = \mathrm{Re}_2 - \mathrm{Re}_1.$$

We have seen directly in (54) that it is only the difference $(\mathrm{Re}_2 - \mathrm{Re}_1)$ that effects marginal stability criterion, i.e., not the individual reduced Reynolds numbers. Also in (54), we may note that the interfacial velocity difference depends strongly on the viscosity ratio κ_1/κ_2 when buoyancy effects are not too large.

In Figs. 7a–d we increase the buoyancy effects via b^*/κ_2. We observe a checker-board effect in the regions of stability and instability. This is not surprising given our choice of variables. For a vertical well, the product

$$[\mathrm{Re}_2 - \mathrm{Re}_1]\left[W_{i,2} - W_{i,1}\right]$$

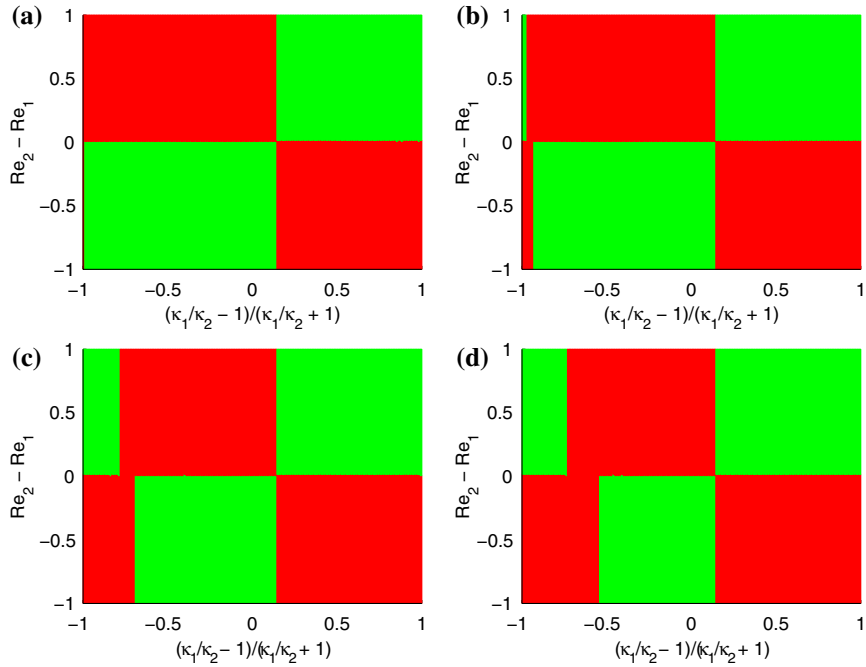

Fig. 8 Regions of marginal stability for a vertical concentric well: $e = 0$, $\beta = 0$, $b^*/\kappa_2 = 1$: (**a**) $\phi_{i,0} = 0.05$; (**b**) $\phi_{i,0} = 0.25$; (**c**) $\phi_{i,0} = 0.75$; (**d**) $\phi_{i,0} = 0.95$; unstable—red (dark), stable—green (light)

has a dominant effect on the stability, as has been discussed above. Changing b^* effects the base flow, (which otherwise depends only on κ_1/κ_2 and $\phi_{i,0}$), and we see the checker-board pattern shifting horizontally. If we had considered the case of zero buoyancy, $b^*/\kappa_2 = 0$, then the equal viscosity case would demarcate between stability and instability.

In Figs. 7e and f, we consider negative buoyancy, $b^* = -1, -2$. As the well is concentric and vertical, changing b^* from positive to negative has essentially no difference on the occurrence of the checkerboard pattern. However, the base flow is changed and this changes the form of checkerboard. We observe that the marginal stability regions are reflected about a vertical axis by the change in sign of the buoyancy. This will not be the case once we consider inclined wells.

Figure 8a–d gives some idea of the effects of changing the interface position, which can be very significant. The primary effect seems to be on the base flow, as we again observe the checker-board pattern, but shifting significantly in the horizontal direction. The loss of symmetry is due to the fact that the layers now have different thicknesses in the azimuthal direction. Fluid layer thickness is known to affect the stability properties of many multi-layer flows; see e.g. many examples in [27, Part 2, Chapter 3].

4.3 Horizontal wells

In a horizontal well there is no effect of buoyancy on the basic flow. Thus we expect that the interfacial velocities always have the same sign. The right-hand side of (54) is thus still checker-boarded with the variables $[\mathrm{Re}_2 - \mathrm{Re}_1]$ and κ_1/κ_2, as before. However, now positive b^* represents a stabilizing azimuthal force on the interface. This effect acts as a threshold that the right-hand side must exceed in order for the flow to be unstable. Graphically, see Fig. 9, we see a rounding of the corners of the unstable regions, and that the unstable regimes recede as b^* increases.

It is also interesting to consider negative b^*, where the heavy fluid lies on top of the lighter fluid in the horizontal well. Surprisingly, it seem in Figs. 9e and f that for suitable choice of reduced Reynolds number difference and

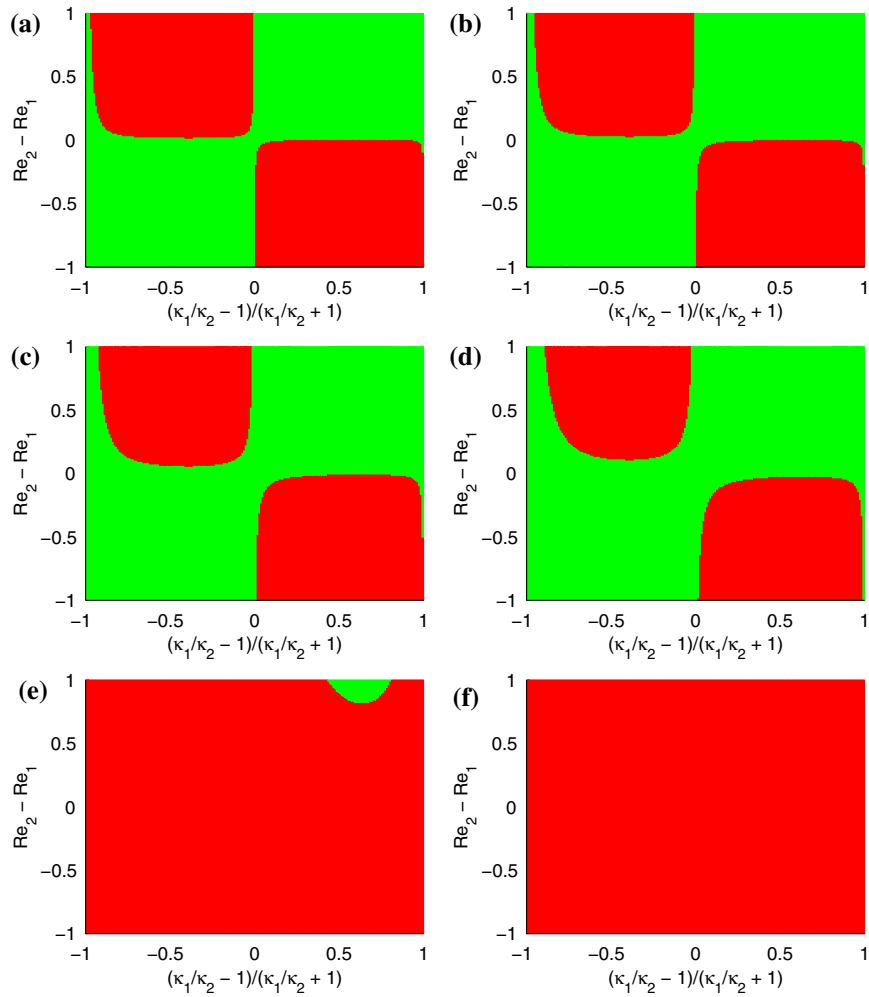

Fig. 9 Regions of marginal stability for a horizontal concentric well: $e = 0$, $\beta = \pi/2$, $\phi_{i,0} = 0.5$: (**a**) $b^*/\kappa_2 = 1$; (**b**) $b^*/\kappa_2 = 2$; (**c**) $b^*/\kappa_2 = 5$; (**d**) $b^*/\kappa_2 = 10$; (**e**) $b^*/\kappa_2 = -1$; (**f**) $b^*/\kappa_2 = -2$; unstable—red (dark), stable—green (light)

viscosity ratio, we are able to stabilize this flow. As we have $\rho_2 < \rho_1$, $\kappa_1 > \kappa_2$ and also $\mathrm{Re}_2 > \mathrm{Re}_1$, it clear that this stabilizing region must be fairly small.

4.4 Inclined wells

Finally, we consider wells at intermediate inclinations, $\beta = \pi/6$ and $\beta = \pi/3$. Now buoyancy is active in both determining the base flow and in providing an azimuthal force to the perturbed flow. The results are shown in Figs. 10 and 11. As should be expected, the results show a continuous transition between the vertical and horizontal results. Again we observe that base flows that are mechanically unstable can be stabilized in a small parameter region.

5 Effects of eccentricity, $e > 0$

We now consider the effects of eccentricity on the flow stability. For eccentric annuli we solve the eigenvalue problem (42)–(48) numerically. In fact, it would be possible to consider a small e expansion, especially as we have

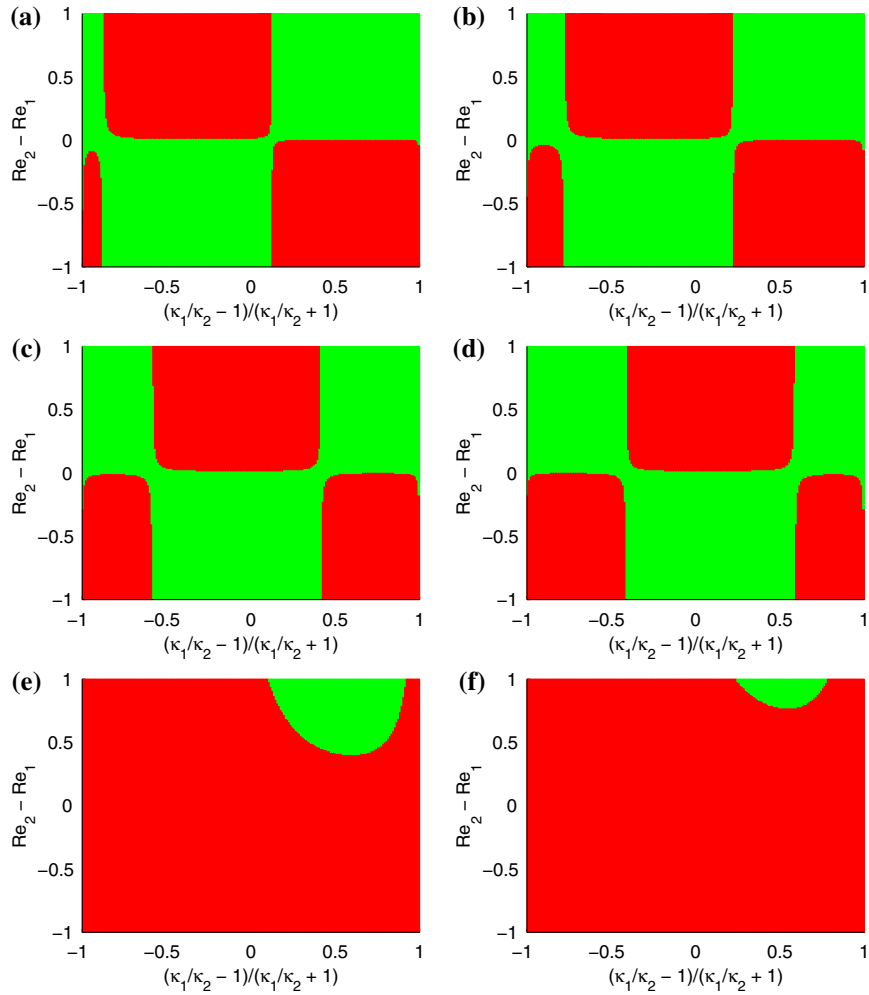

Fig. 10 Regions of marginal stability for an inclined concentric well: $e = 0$, $\beta = \pi/6$, $\phi_{i,0} = 0.5$: (**a**) $b^*/\kappa_2 = 1$; (**b**) $b^*/\kappa_2 = 2$; (**c**) $b^*/\kappa_2 = 5$; (**d**) $b^*/\kappa_2 = 10$; (**e**) $b^*/\kappa_2 = -1$; (**f**) $b^*/\kappa_2 = -2$; unstable—red (dark), stable—green (light)

the full solution for the base flow expressed analytically in (21) and (22), and this takes the form of a power series in e. This approach has been used in [5,7] for other annular displacement problems.

For computational solution of (42)–(48) we use a spectral method. These are global methods that use the fully discretized stability operator, which is supplied to a matrix eigenvalue solver to give the spectrum. We have chosen a Chebyshev polynomial expansion to discretize our problem. The use of Chebyshev polynomials, especially in bounded domains, has proven very effective and accurate for such problems. The implementation of the method for our problem is fairly standard, and we refer to [28, pp. 479–508] for details of similar implementations for (more complex) hydrodynamic stability problems. As a test problem we were able to validate our code against the analytical solution for a concentric annulus.

5.1 Example results

Taking the same base parameters as for Fig. 6, we now explore the effects of a gradual increase in eccentricity. The analogous results to Fig. 6, for eccentricities $e = 0.1,\ 0.3,\ 0.5,\ 0.8$ are shown in Figs. 13–15, respectively. There are some interesting observations to be made.

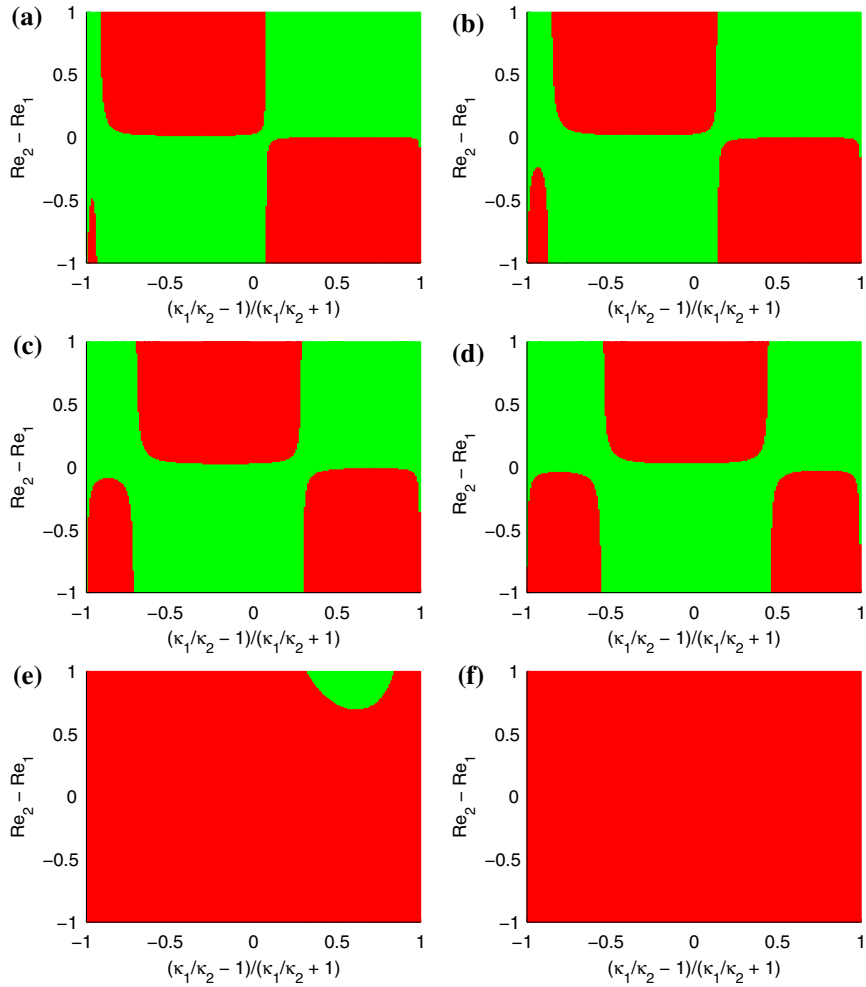

Fig. 11 Regions of marginal stability for an inclined concentric well: $e = 0$, $\beta = \pi/3$, $\phi_{i,0} = 0.5$: (**a**) $b^*/\kappa_2 = 1$; (**b**) $b^*/\kappa_2 = 2$; (**c**) $b^*/\kappa_2 = 5$; (**d**) $b^*/\kappa_2 = 10$; (**e**) $b^*/\kappa_2 = -1$; (**f**) $b^*/\kappa_2 = -2$; unstable—red (dark), stable—green (light)

Firstly, although changing eccentricity does result in changes in $s_{I,\max}/\epsilon$, the classification of the flow as being stable or unstable does not appear to be affected significantly by the eccentricity. Note, however, that we have chosen one fixed value of $\mathrm{Re}_2 - \mathrm{Re}_1$ for these plots and therefore it is difficult to draw general conclusions. We investigate parametric dependence more widely in Sect. 5.3 below.

As the eccentricity increases and when the well is progressively inclined we observe that over some range of small α, $s_{I,\max}/\epsilon$ appears to be independent of the viscosity ratio for stable modes. This is visible in Figs. 12c–15c and Figs. 12d–15d. It is unclear why this is. Another effect we can see at large α is that the stable modes become independent of α; see e.g. the horizontal lines in Fig. 14. This is not a numerical artefact. In Fig. 16 we show the evolution of the spectrum with α for $\alpha \in [1, 15]$. The typical spectrum consists of two sequences of stable discrete modes with $s_I/\epsilon < 0$, and two individual interfacial modes. The sequences of stable modes correspond to the viscous modes of the single fluid problem in each fluid layer and the interfacial modes come from the jump condition. The interfacial modes may be either positive or negative.

Figure 16 shows only one sequence of viscous modes and one interfacial mode. The second sequence of viscous modes and the second interfacial mode are more stable than those shown. We illustrate the variation in the interfacial mode with the dashed line for all $\alpha \in [1, 15]$, but the viscous modes we plot only at $\alpha = 1$ (marked with ∘) and

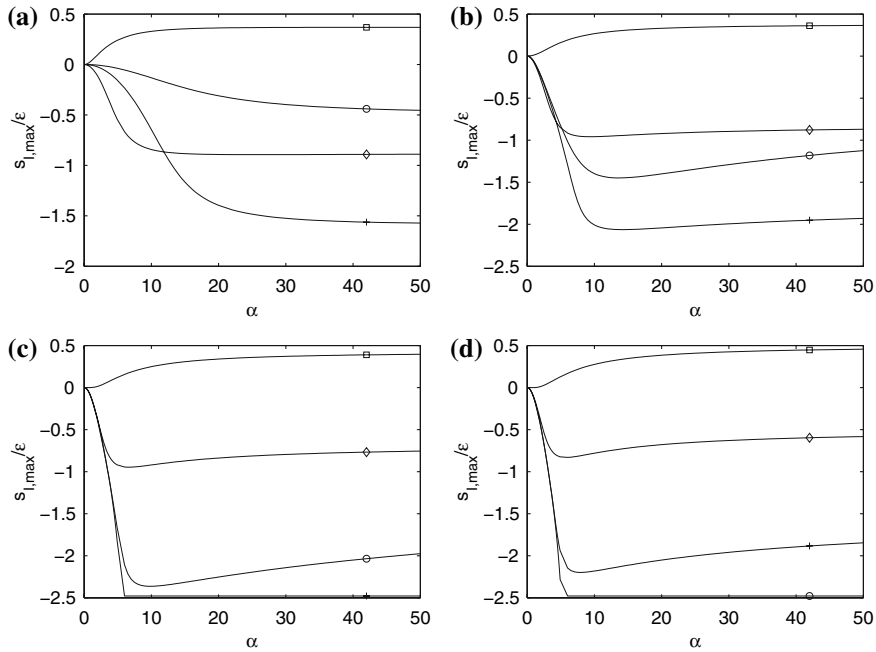

Fig. 12 Examples of typical variations in least stable eigenvalue with wavenumber in a eccentric annulus, $e = 0.1$: $\phi_{i,0} = 0.5$, $b^*/\kappa_2 = 1$, $\mathrm{Re}_1 = 1.0$, $\mathrm{Re}_2 = 0.5$; (**a**) $\beta = 0$; (**b**) $\beta = \pi/6$; (**c**) $\beta = \pi/3$; (**d**) $\beta = \pi/2$. In each figure $\kappa_1/\kappa_2 = 0.02$—marked with o, $\kappa_1/\kappa_2 = 0.1$—marked with +, $\kappa_1/\kappa_2 = 0.5$—marked with $\diamond$, $\kappa_1/\kappa_2 = 2.5$—marked with $\square$

$\alpha = 15$ (marked with $\square$). The viscous modes for $\alpha = 15$ are offset by 0.5 along the real axis for clarity, i.e., the spectra displayed approximately overlay one another. Thus, the viscous modes typically lie along the imaginary axis with small real parts, positive and negative. We can see that the range of s_I/ϵ of the viscous modes is apparently not affected much by changes in α. The interfacial modes typically have positive real part, (unless buoyancy effects are very large), corresponding to advection in the kinematic equation.

The horizontal part of curves in Figs. 12–15 for some of the stable modes is now explained, with reference to Fig. 16a, where we have shown a stable interfacial mode corresponding to the same parameters as in Fig. 14a for $\kappa_1/\kappa_2 = 0.5$. We see that at large α the interfacial mode becomes more stable than the least stable of the viscous modes, which is relatively insensitive at large α. Figure 16b shows an unstable case, $\kappa_1/\kappa_2 = 2.5$.

5.2 Long-wavelength approximation

Although we have seen that computing the spectrum is straightforward, it involves numerical solution of a matrix eigenvalue problem. In situations where one would want to rapidly and frequently assess the stability of the flow, (e.g. as part of a process simulation), this may be too time consuming. In such situations, one could use the long-wavelength approximation to (42)–(48), which allows an analytical solution and provides sufficient conditions for instability.

The size of the growth rate for wavenumbers $\alpha \sim O(1)$ is not necessarily well predicted by the long-wavelength approximation, but anyway we have seen that $O(1)$ growth rates are commonly found when the flow is unstable. An alternative analytic limit is the short-wavelength limit $\alpha \to \infty$. Although we could consider this limit, we note that the Hele-Shaw model averages over the annular gap. Hence at wavelengths that are comparable with the annular gap length-scale, the validity of the displacement model becomes questionable.

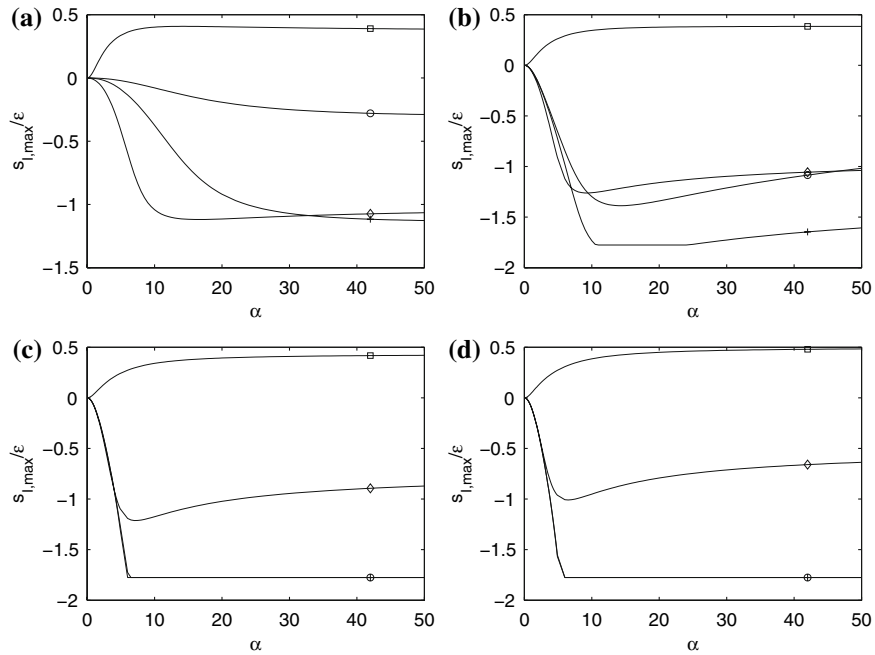

Fig. 13 As Fig. 12 but with $e = 0.3$

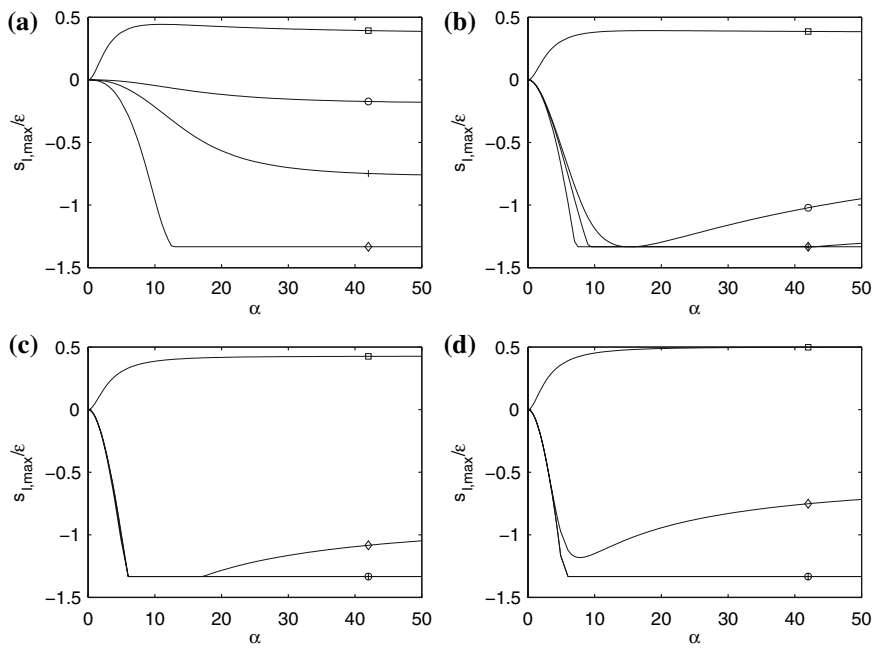

Fig. 14 As Fig. 12 but with $e = 0.5$

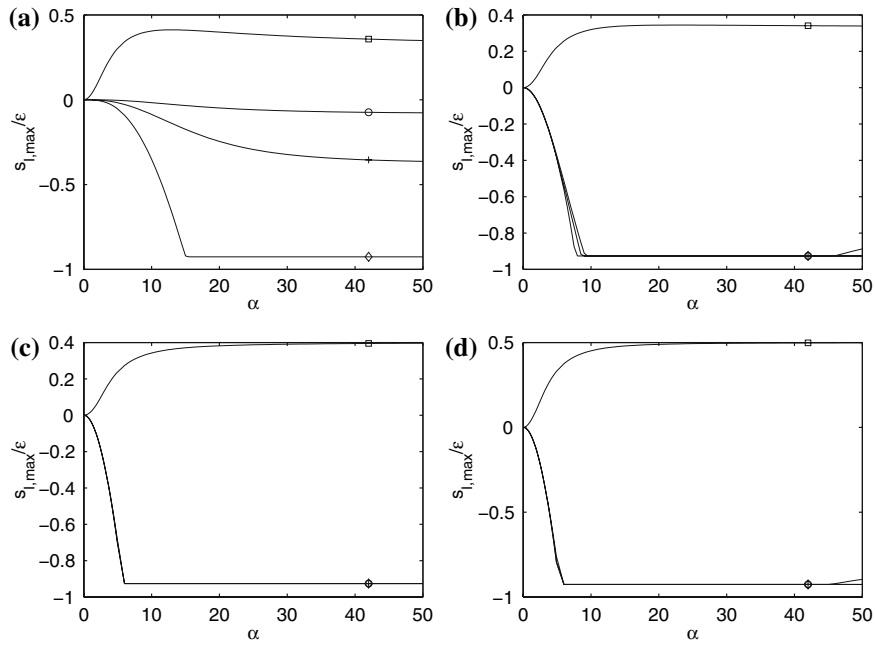

Fig. 15 As Fig. 12 but with $e = 0.8$

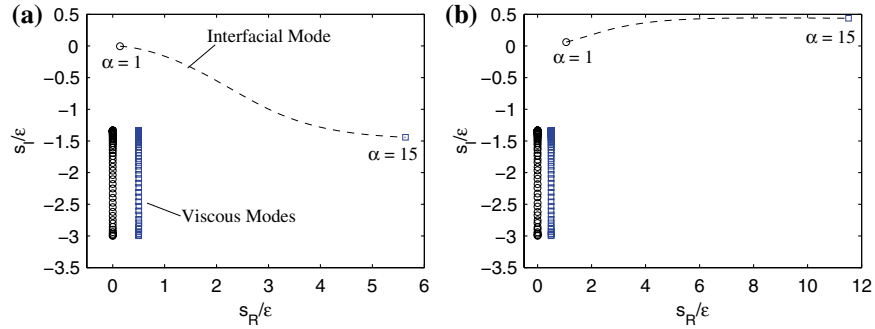

Fig. 16 Evolution of the spectrum with α: viscous modes and interfacial mode for $e = 0.5$, $\phi_{i,0} = 0.5$, $b^*/\kappa_2 = 1$, $\mathrm{Re}_1 = 1.0$, $\mathrm{Re}_2 = 0.5$, $\beta = 0$; (**a**) $\kappa_1/\kappa_2 = 0.5$; (**b**) $\kappa_1/\kappa_2 = 2.5$. Each figure shows variation in interfacial mode for $\alpha \in [1, 15]$ and viscous modes at $\alpha = 1$ (marked with ○) and $\alpha = 15$ (marked with □); the viscous modes for $\alpha = 15$ are offset by 0.5 along the real axis

The long-wavelength limit, $\alpha \to 0$, is studied by assuming a regular perturbation expansion in α for both s/ϵ and the solution to (42)–(48). After considerable algebra we find the following expressions:

$$\frac{s}{\epsilon} \sim \alpha \frac{s_1}{\epsilon} + i\alpha^2 \frac{s_2}{\epsilon} + O(\alpha^3), \tag{55}$$

$$\frac{s_1}{\epsilon} = \frac{M_1 W_{i,2} + M_2 W_{i,1}}{M_1 + M_2}, \tag{56}$$

$$\frac{s_2}{\epsilon} = \mathrm{i}\left\{ -\frac{(b/\kappa_2)\tan\beta \sin\pi\phi_{i,0}}{3\pi H(\phi_{i,0})(\kappa_1/\kappa_2)} \left[\frac{M_1 M_2}{M_1 + M_2}\right] + \frac{s_1}{\epsilon}\frac{(W_{i,2} - W_{i,1})}{3} \left[\frac{\mathrm{Re}_1 N_1 M_2 - \mathrm{Re}_2 N_2 M_1}{(M_1 + M_2)^2}\right] \right\}, \tag{57}$$

where

$$M_1 = \pi \int_0^{\phi_{i,0}} H^3(\phi)\mathrm{d}\phi = P(\phi_{i,0}, e),$$

$$M_2 = \pi \frac{\kappa_1}{\kappa_2} \int_{\phi_{i,0}}^1 H^3(\phi)\mathrm{d}\phi = \frac{\kappa_1}{\kappa_2}[P(1, e) - P(\phi_{i,0}, e)],$$

$$N_1 = \pi \int_0^{\phi_{i,0}} H^5(\phi)\mathrm{d}\phi = Q(\phi_{i,0}, e),$$

$$N_2 = \pi \frac{\kappa_1}{\kappa_2} \int_{\phi_{i,0}}^1 H^5(\phi)\mathrm{d}\phi = \frac{\kappa_1}{\kappa_2}[Q(1, e) - Q(\phi_{i,0}, e)].$$

The function $P(\phi, e)$ is defined in (23), in relation to the base flow, and $Q(\phi, e)$ is a quintic in e, given by:

$$\begin{aligned} Q(\phi, e) = {} & \pi\phi + 5e \sin \pi\phi + 5e^2[\pi\phi + \cos \pi\phi \sin \pi\phi] + \frac{10e^3}{3}[\cos^2 \pi\phi \sin \pi\phi + 2 \sin^3 \pi\phi] \\ & + \frac{5e^4}{4}\left[\cos^3 \pi\phi \sin \pi\phi + \frac{3}{2}(\pi\phi + \cos \pi\phi \sin \pi\phi)\right] \\ & + \frac{e^5}{5}\left[\cos^4 \pi\phi \sin \pi\phi + \frac{4}{3}(\cos^2 \pi\phi \sin \pi\phi + 2 \sin^3 \pi\phi)\right]. \end{aligned} \tag{58}$$

We note that the first-order eigenfunction s_1/ϵ is real. We can see that s_1/ϵ is given simply as a weighted average of the interfacial velocities of the two fluid layers. Provided that axial buoyancy effects are not severe, (i.e., b not too large) we would expect the interfacial velocities to have the same (positive) sign and hence we see that the leading-order effect is advection at a mean interfacial speed. The stability of the flow is thus determined at second order, where we note that s_2/ϵ is pure imaginary.

The first term in (57) contains the effects of azimuthal buoyancy, which we see are stabilizing when $b > 0$, as before. The second term is more complex. Let us suppose that buoyancy effects are modest, so that the interfacial velocities are both positive. Then $s_1/\epsilon > 0$ and we see that the second term is stabilizing only if the interfacial velocity difference $(W_{i,2} - W_{i,1})$ has the same sign as:

$$\mathrm{Re}_2 N_2 M_1 - \mathrm{Re}_1 N_1 M_2,$$

which is a weighted difference in the reduced Reynolds numbers of the two flows. Destabilization occurs when these have opposite sign. This situation is therefore physically similar to that for the concentric annulus that we have discussed at length.

We note that to evaluate the long-wavelength limit, only the base flow is required, plus the functionals M_k and N_k. Each of these can be calculated analytically, and therefore the long-wavelength limit is very fast to compute for either parametric study or inclusion in a more complex model.

5.3 Long-wavelength approximation: parametric results

For fixed positive buoyancy parameter, $b^*/\kappa_2 = 1$, we explore below the effects of eccentricity at different inclinations: $\beta = 0,\ \pi/6,\ \pi/3,\ \pi/2$, as before. We fix the interface position at mid-azimuth, $\phi_{i,0} = 0.5$. As with the concentric annulus, we explore variations with κ_1/κ_2. We have seen in (57) that it is a weighted average of the Reynolds number difference that governs stability. Therefore, we plot on the y-axis the difference $d(\mathrm{Re}_2, \mathrm{Re}_1, e)$:

$$d(\mathrm{Re}_2, \mathrm{Re}_1, e) = \frac{\mathrm{Re}_2 N_2 M_1 - \mathrm{Re}_1 N_1 M_2}{(M_1 + M_2)^2}.$$

In a vertical well, see Fig. 17, increasing eccentricity seems to simply cause a shift in the checkerboard pattern from the concentric case in Fig. 7a. We see that depending on κ_1/κ_2 and on $d(\mathrm{Re}_2, \mathrm{Re}_1, e)$, changes in eccentricity could be either stabilizing or destabilizing. Note however that $d(\mathrm{Re}_2, \mathrm{Re}_1, e)$ varies nonlinearly with e from the

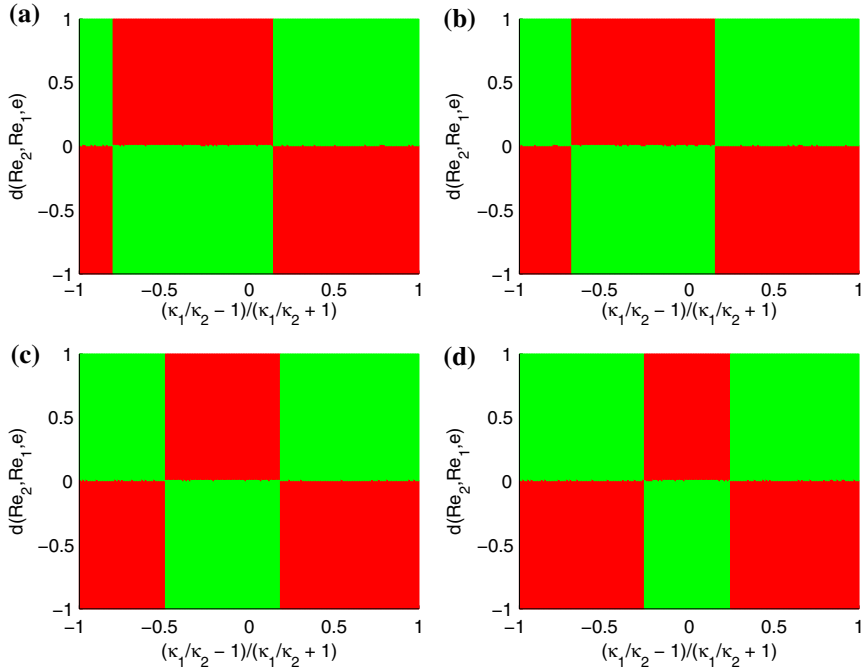

Fig. 17 Regions of marginal stability for an eccentric annulus, long-wavelength approximation: $\beta = 0$, $b^*/\kappa_2 = 1$, $\phi_{i,0} = 0.5$: (**a**) $e = 0.1$; (**b**) $e = 0.25$; (**c**) $e = 0.5$; (**d**) $e = 0.8$; unstable—red (dark), stable—green (light)

difference $\mathrm{Re}_2 - \mathrm{Re}_1$ at $e = 0$. The checker-boarding is evident from (57) as the azimuthal buoyancy term is not present in a vertical well. The change in checker-boarding pattern at fixed $d(\mathrm{Re}_2, \mathrm{Re}_1, e)$ is due only to a change in the base flow.

As both the annulus inclination and the eccentricity increase, Figs. 18–20, we see a marked increase in stability. Such that for the horizontal annulus all physically realisable conditions are stable. Note that for an eccentric annulus the geometric constants N_k, M_k satisfy $M_1 N_2 > N_1 M_2$, and that the bottom right-hand corner of these figures requires: $\kappa_1/\kappa_2 > 1$ while also $\kappa_1/\kappa_2 < (\rho_1/\rho_2)(N_1 M_2)/(M_1 N_2) < 1$ for $b^*/\kappa_2 > 0$, i.e., although well defined mathematically, these parameters cannot be physically attained.

For a fixed inclination of $\beta = \pi/6$ we consider variations in the stability with interface position. At $\phi_{i,0} = 0.75$, see Fig. 21, the heavier fluid lies on the low side of the annulus in a thinner layer than in Fig. 18, ($\phi_{i,0} = 0.5$). The effect appears to be to stabilize the flow. Conversely, as the interface moves to the wide side of the annulus, $\phi_{i,0} = 0.25$, the flow is less stable; see Fig. 22. It appears that, in order to destabilize the narrow side of the annulus, when significantly eccentric, we need a negative density difference, i.e., so that the heavy fluid is driven around to the narrow side. This is indeed found to be the case. Figure 23 shows the same configuration as Fig. 21, but with $b^*/\kappa_2 < 0$. A negative density difference clearly has a significant effect.

6 Discussion

We have shown a variety of new results in this paper. In the first place we have presented the analytical solution for the parallel flow of two Newtonian fluids of differing physical properties in an eccentric annulus, in the narrow gap limit. This solution depends on four dimensionless parameters. Secondly, we have shown that the stability of this flow can be characterized by these four parameters and three additional dimensionless parameters, plus a wavenumber of the disturbance. In those cases that are amenable to analysis, e.g. concentric annulus and long-wavelength limit, it appears that at least one of these parameters is redundant as it is a (geometrically scaled) difference in

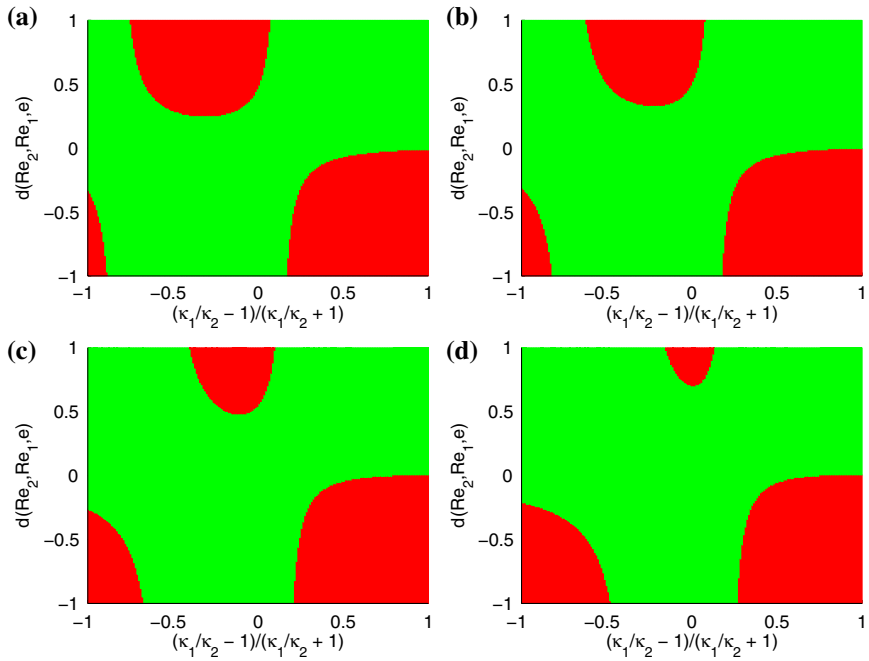

Fig. 18 As Fig. 17 except $\beta = \pi/6$

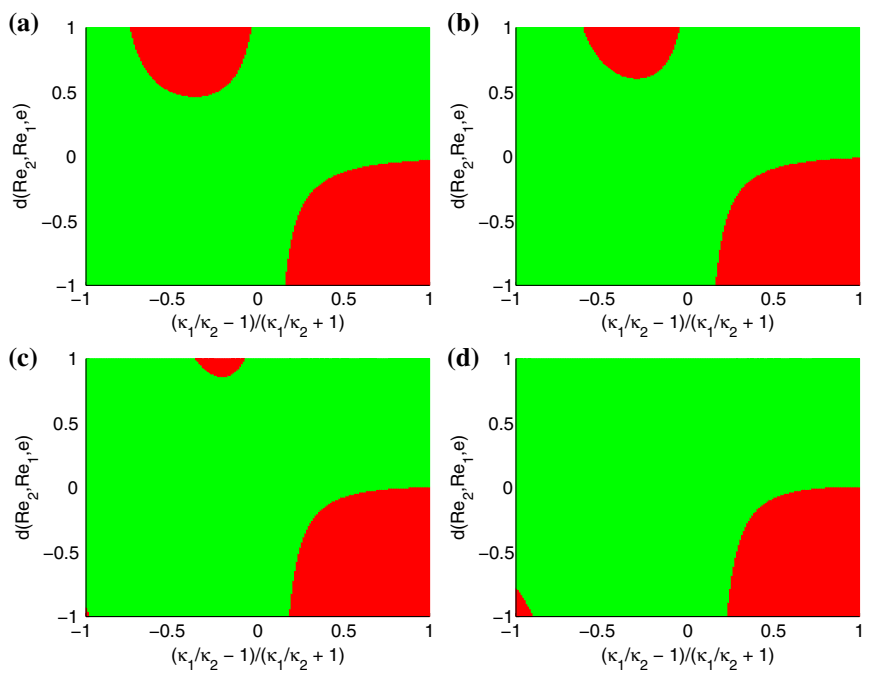

Fig. 19 As Fig. 17 except $\beta = \pi/3$

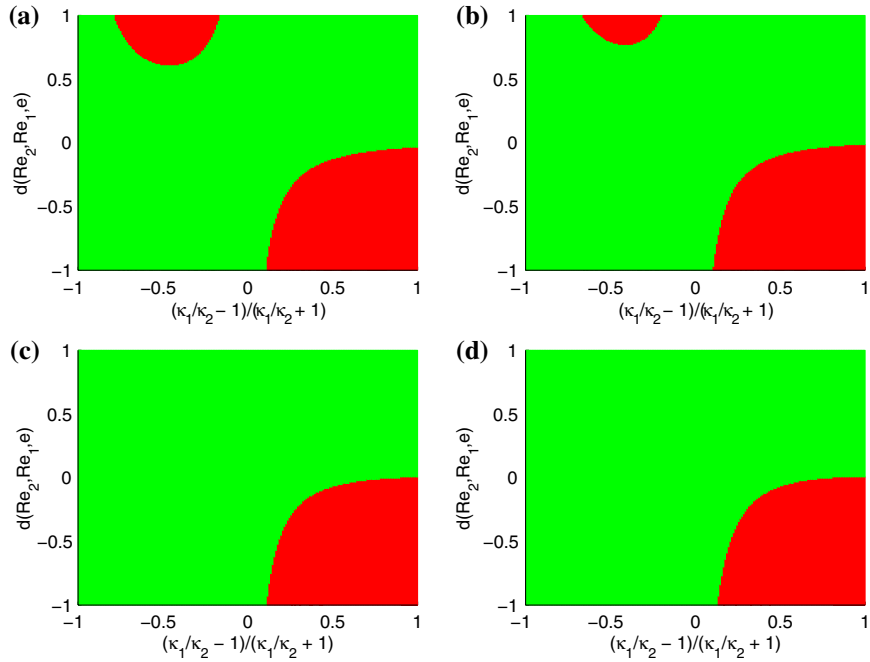

Fig. 20 As Fig. 17 except $\beta = \pi/2$

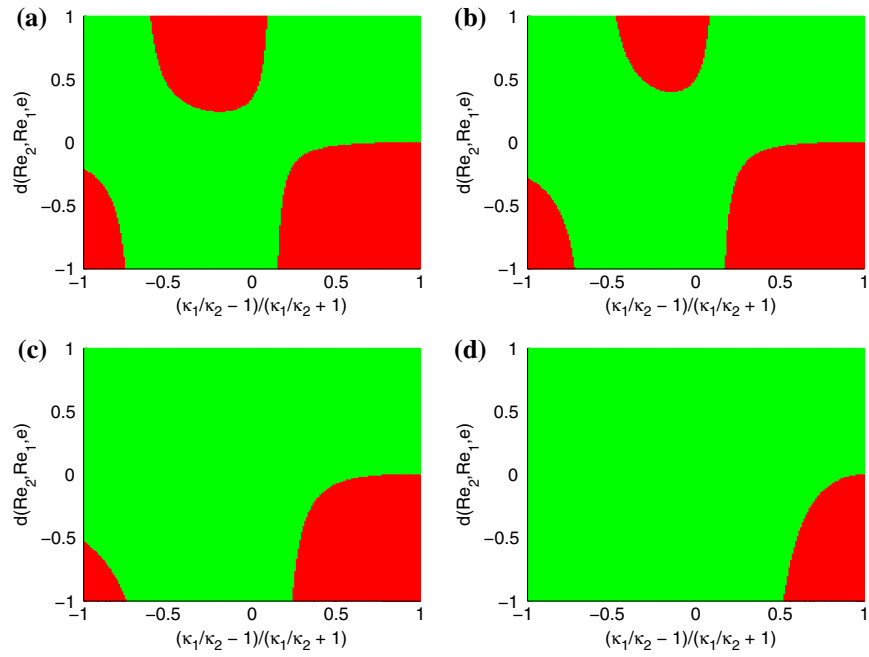

Fig. 21 As Fig. 18 except $\phi_{i,0} = 0.75$

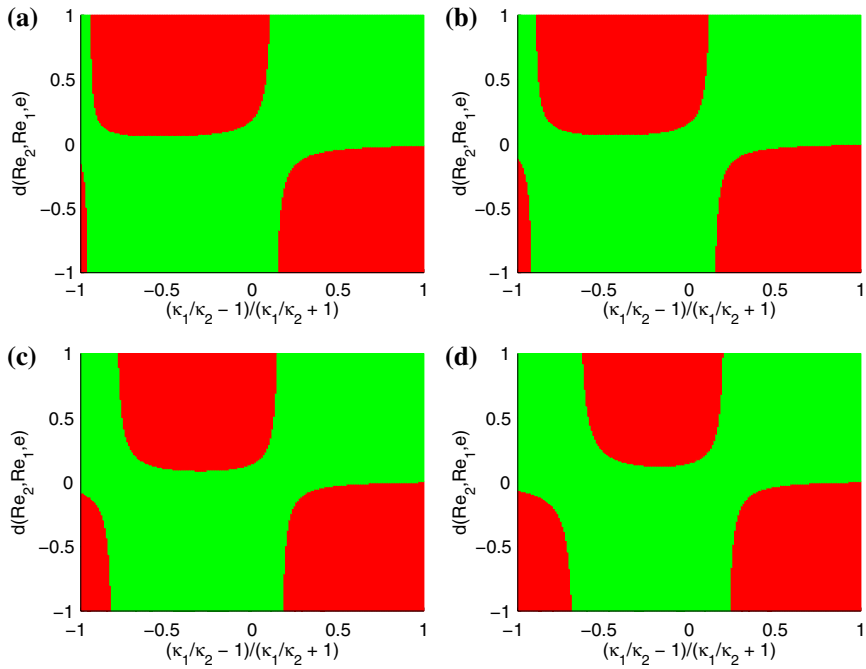

Fig. 22 As Fig. 18 except $\phi_{i,0} = 0.25$

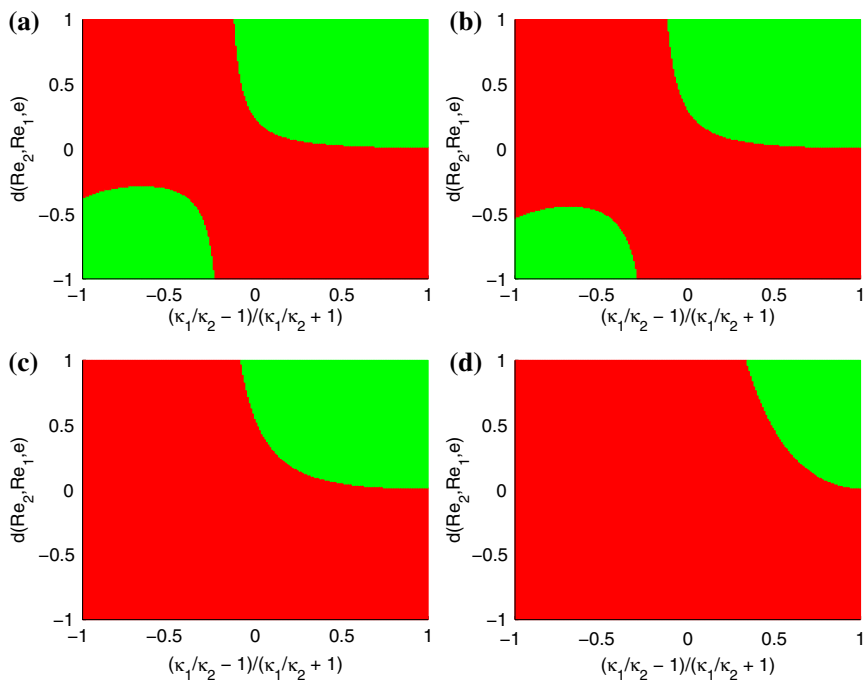

Fig. 23 As Fig. 17 except $\beta = \pi/6$, $b^*/\kappa_2 = -1$, $\phi_{i,0} = 0.75$

Reynolds numbers that controls stability and not the individual Reynolds numbers. Thus, at its simplest we may say that the stability of this flow is governed by six dimensionless parameters.

Our analysis has no surface tension included, as the oilfield fluids involved are often miscible. Thus, although the interfacial velocities play a large part in the analysis and we have shown that it is an interfacial mode that first becomes unstable, the instability is not a classical "interfacial instability", due to the omission of surface tension. Rather, it is the kinematic equation that allows the instabilities. Hence, we may refer to these as kinematic instabilities.

For concentric annuli we may summarize the results as follows. At low buoyancy levels, instability results when the difference in interfacial velocities and the difference in reduced Reynolds numbers are sufficiently strong and of different sign. The interfacial velocity jump (at low fixed buoyancy) can be related to a jump in the dynamic viscosity whereas the difference in reduced Reynolds numbers corresponds to a jump in the kinematic viscosity. Viewed differently, we might consider that the jump in the interfacial velocity of the base flow is the destabilizing source of energy. If for example $W_{i,2} - W_{i,1} > 0$, we might expect that energy is transferred primarily from the fluid 2 stream to the fluid 1 stream. If now $\kappa_1/\rho_1 > \kappa_2/\rho_2$, then fluid 1 is more able to dissipate this energy via viscous diffusion, than fluid 2. Thus, we might argue that this configuration is stabilizing, (note that this corresponds to a positive difference in reduced Reynolds number). Conversely, if $\kappa_1/\rho_1 < \kappa_2/\rho_2$, fluid 1 cannot diffuse the energy as well as fluid 2 and hence the flow destabilizes. At large buoyancies, the averaged interfacial speed can change sign, which has the effect of reversing the direction of advection of the perturbation and also the stability. This effect is partly responsible for the checkerboarding.

Once eccentricity is introduced, with a positive density difference and even a small inclination from vertical, the flow becomes increasingly stable. The stability increases with azimuthal position of the interface. For negative density differences, increases in eccentricity appear to have the opposite effect.

In many results such as those in Figs. 6 and 12–15 we observed that the least-stable modes were found in the short-wavelength limit, $\alpha \to \infty$. For other parameters, the long-wavelength limit gave the most stable maximal s_I. In the case of instability this suggests that the Hele-Shaw type model will become invalid, since wavelengths of the order of the gap-thickness are excited. As soon as such modes are excited the model assumptions on scaling break down and a three-dimensional analysis is called for to fully resolve the instability. As always, linear stability is necessary for a flow to be stable but linear instability is sufficient for flow instability. We have not yet studied the three-dimensional stability problem.

In comparison to previously published work, some of our results are qualitatively similar. For example, the appearance of an averaged (interfacial) velocity in the dispersion relation and the effect of azimuthal buoyancy are quite similar to those in the problems considered by [16–18,20,21]. However, the physical orientation we consider is significantly different. Here the base flow is coupled both via the jump conditions and constrained by the imposed flow rate. In the annular geometry, the magnitude of the gravitational buoyancy force that acts perpendicular to the interface depends not only on annular inclination, but also on the interface azimuthal position. The eccentricity effects both viscous dissipation and acceleration of perturbation (viscous terms scale like H^{-3} and acceleration terms scale like H^{-1}). Eccentricity also naturally causes a velocity differences in the base flow.

Finally, in terms of the practical implications of our work. We have seen that eccentricity of the annulus can have a powerful effect on stabilising the flow when the buoyancy difference is positive. There are certainly cases when this occurs, e.g. when the displacing fluid is a light spacer or wash, that channels rapidly past the drilling mud up the wide side of the annulus. Our analysis predicts that such flows will be interfacially stable and here "stable" means that the displacement will be poor.

In order to have instabilities at significant eccentricities or inclinations, we require that the displacing fluid on the wide side be heavier than that on the narrow side. Conventional practice, see [8], suggests that a hierarchy of both density and viscosity differences is required for a good displacement in a near vertical well, i.e., in which no channelling occurs. Our results suggest that if one is unable to ensure both a positive density difference and a positive viscosity difference, it may be better to compromise the viscosity difference. In this case, if the displacing fluid channels up the wide side of the annulus, it may still destabilize the narrow side and mix azimuthally as a long finger develops. For horizontal wells the balance is far more delicate, as any density difference is likely to cause

stable stratification. Here the only suggestion is to design the viscosity of the displacing fluid and try to match the fluid densities as far as possible. A final word of caution is that our results in this paper consider only Newtonian fluids, whereas real wellbore fluids are typically shear thinning and possess a yield stress. This is the subject of our companion paper.

Acknowledgements This research has been carried out at the University of British Columbia, supported financially by Schlumberger and NSERC through CRD project 245434. We are grateful for this sponsorship. We thank Stefan Storey for provision of Fig. 4, illustrating the narrow side instabilities.

References

1. Economides MJ (1990) Implications of cementing on well performance. In: Nelson EB (ed) Well cementing. Schlumberger Educational Services
2. Primary and Remedial Cementing Guidelines. Drilling and Completions Committee, Alberta, April 1995. Distributed by the Petroleum Industry Training Service
3. Nelson EB (ed) (2001) Well cementing. Schlumberger Educational Services
4. Bittleston SH, Ferguson J, Frigaard IA (2002) Mud removal and cement placement during primary cementing of an oil well; laminar non-Newtonian displacements in an eccentric annular Hele-Shaw cell. J Engng Math 43:229–253
5. Pelipenko S, Frigaard IA (2004) On steady state displacements in primary cementing of an oil well. J Engng Math 46(1):1–26
6. Pelipenko S, Frigaard IA (2004) Two-dimensional computational simulation of eccentric annular cementing displacements. IMA J Appl Math 64(6):557–583
7. Pelipenko S, Frigaard IA (2004) Visco-plastic fluid displacements in near-vertical narrow eccentric annuli: prediction of travelling wave solutions and interfacial instability. J Fluid Mech 520:343–377
8. Guillot D, Hendriks H, Callet F, Vidick B (1990) Mud Removal. In: Nelson EB (ed) Well cementing. Schlumberger Educational Services
9. Lockyear CF, Ryan DF, Gunningham MM (1989) Cement channelling: how to predict and prevent. Society of Petroleum Engineers paper number SPE 19865
10. McLean RH, Manry CW, Whitaker WW (1966) Displacement mechanics in primary cementing. Society of Petroleum Engineers paper number SPE 1488
11. Moyers-González MA (2006) Transient effects in oilfield cementing flows. Dissertation, University of British Columbia
12. Moyers-González MA, Frigaard IA, Scherzer O, Tsai T-P (2007) Transient effects in oilfield cementing flows: Qualitative behaviour. Euro J Appl Math 18:477–512
13. Tehrani A, Ferguson J, Bittleston SH (1992) Laminar displacement in annuli: a combined experimental and theoretical Study. Society of Petroleum Engineers paper number SPE 24569
14. Tehrani A, Bittleston SH, Long PJG (1993) Flow instabilities during annular displacement of one non-Newtonian fluid by another. Exp Fluids 14:246–256
15. Homsy GM (1987) Viscous fingering in porous media. Annu Rev Fluid Mech 19:271–311
16. Raghavan R, Marsden SS (1973) A theoretical study of the instability in the parallel flow of immiscible liquids in a porous medium. Quart J Mech Appl Math 26:205–216
17. Zeybek M, Yortsos YC (1991) Long waves in parallel flow in Hele-Shaw cells. Phys Rev Lett 67:1430–1433
18. Zeybek M, Yortsos YC (1992) Parallel flow in Hele-Shaw cells. J Fluid Mech 244:421–442
19. Miranda JO, Widom M (2000) Parallel flow in Hele-Shaw cells with ferrofluids. Phys Rev E 61:2114–2117
20. Gondret P, Rakotomalala N, Rabaud M, Salin D, Watzky P (1997) Viscous parallel flows in finite aspect ratio Hele-Shaw cell: Analytical and numerical results. Phys Fluids 9(6):1841–1843
21. Gondret P, Rabaud M (1997) Shear instabillity of two-fluid parallel flow in a Helle-Shaw cell. Phys Fluids 9(11):3267–3274
22. Gondret P, Ern P, Meignin L, Rabaud M (1999) Experimental evidence of a nonlinear transition from convective to absolute Instability. Phys Rev Lett 82(7):1442–1447
23. Hinch EJ, Plouraboué F (2005) Kelvin-Helmholtz instability in a Hele-Shaw cell: Large effect from the small region near the meniscus. Phys Fluids 17:052107(13 pages)
24. Meignin L, Ern P, Gondret P, Rabaud M (2001) Gap size effects for the Kelvin-Helmholtz instability in a Hele-Shaw cell. Phys Rev E 64:026308
25. Meignin L, Gondret P, Ruyer-Quil C, Rabaud M (2003) Subcritical Kelvin-Helmholtz Instability in a Hele-Shaw Cell. Phys Rev Lett 90:234502
26. Plouraboué F, Hinch EJ (2002) Kelvin-Helmholtz instability in a Hele-Shaw cell. Phys Fluids 14(3):922–929
27. Joseph DD, Renardy YY (1993) Fundamentals of two-fluid dynamics. Interdisciplinary Applied Mathematics, Springer
28. Schmid PJ, Henningson DS (2001) Stability and transition in shear flows. Springer-Verlag, New York, Inc